International Journal of Biological Macromolecules 279 (2024) 135271

Contents lists available at ScienceDirect

International Journal of Biological Macromolecules

journal homepage: www.elsevier.com/locate/ijbiomac

Hyaluronic acid-covered ferric ion-rich nanobullets with high zoledronic acid payload for breast tumor-targeted chemo/chemodynamic therapy

Nien-Tzu Yeh [a], Tzu-Chen Lin [a], I-Ju Liu [a], Shang-Hsiu Hu [b], Tsai-Ching Hsu [c,d,e], Hao-Yang Chin [c], Bor-Show Tzang [c,d,e,f,*], Wen-Hsuan Chiang [a,**]

[a] Department of Chemical Engineering, i-Center for Advanced Science and Technology (iCAST), National Chung Hsing University, Taichung 402, Taiwan
[b] Department of Biomedical Engineering and Environmental Sciences, National Tsing Hua University, Hsinchu 300, Taiwan
[c] Institute of Medicine, Chung Shan Medical University, Taichung 402, Taiwan
[d] Immunology Research Center, Chung Shan Medical University, Taichung 402, Taiwan
[e] Department of Clinical Laboratory, Chung Shan Medical University Hospital, Taichung 402, Taiwan
[f] Department of Biochemistry, School of Medicine, Chung Shan Medical University, Taichung 402, Taiwan

ARTICLE INFO

Keywords:
Zoledronic acid
Metal-organic frameworks
Nanobullets
Hyaluronic acid
Tumor-targeted chemo/chemodynamic therapy

ABSTRACT

Due to the heterogeneity of the tumor microenvironment, the clinical efficacy of tumor treatment is not satisfied, highlighting the necessity for new strategies to tackle this issue. To effectively treat breast tumors by tumor-targeted chemo/chemodynamic therapy, herein, the Fe^{3+}-rich MIL-88B nanobullets (MNs) covered with hyaluronic acid (HA) were fabricated as vehicles of zoledronic acid (ZA). The attained ZA@HMNs showed a high ZA payload (ca 29.6 %), outstanding colloidal stability in the serum-containing milieu, and accelerated ZA as well as Fe^{3+} release under weakly acidic and glutathione (GSH)-rich conditions. Also, the ZA@HMNs consumed GSH by GSH-mediated Fe^{3+} reduction and converted H_2O_2 into •OH via Fenton or Fenton-like reaction with pH reduction. After being internalized by 4T1 cells upon CD44-mediated endocytosis, the ZA@HMNs depleted intracellular GSH and degraded H_2O_2 into •OH, thus eliciting lipid peroxidation and mitochondria damage to suppress cell proliferation. Also, the ZA@HMNs remarkably killed macrophage-like RAW 264.7 cells. Importantly, the in vivo studies and ki67 and GPX4 staining of tumor sections demonstrated that the ZA@HMNs efficiently accumulated in 4T1 tumors to hinder tumor growth via ZA chemotherapy combined with •OH-mediated ferroptosis. This work presents a practicable strategy to fabricate ZA@HMNs for breast tumor-targeted chemo/chemodynamic therapy with potential clinical translation.

1. Introduction

Nowadays, cancer, as a major killer, has threatened largely human health and living quality [1,2]. For women, the most commonly diagnosed cancer and a leading cause of cancer death is breast cancer, whereas it is lung cancer for men [3–5]. Patients with advanced breast cancer frequently develop bone metastases, and at this stage, the disease is considered incurable [6,7]. The antiresorptive zoledronic acid (ZA), a third-generation bisphosphonate, has been administered to breast cancer patients and has obtained good outcomes in preventing bone metastases [8,9]. Different from the first-generation bisphosphonates (e.g. etidronate), ZA impedes bone resorption by directly inhibiting farnesyl diphosphate synthase (FPPS), a significant enzyme of the mevalonate pathway [9–11]. Note that the ZA-mediated FPPS inhibition has been demonstrated to suppress cell proliferation and migration, thus leading to apoptosis [12,13]. Furthermore, as shown in a previous clinical trial of early-stage breast cancer patients, the adjuvant bisphosphonate treatment declined not only the risk of cancer metastasis to bones but also the possibility of getting secondary cancers [13,14], which could be correlated to the direct anticancer effects of ZA [11]. Several studies further reported the prominent capability of ZA in specific tumor-associated macrophage (TAM) killing and TAM phenotype remodeling [15–18].

Encouraged by the aforementioned findings, the use of ZA to treat extraskeletal tumors has attracted considerable attention in the past decade [7,13,19–23]. However, due to the extensive renal clearance

* Correspondence to: B.-S. Tzang, Institute of Medicine, Chung Shan Medical University, Taichung 402, Taiwan.
** Corresponding author.
E-mail addresses: bstzang@csmu.edu.tw (B.-S. Tzang), whchiang@dragon.nchu.edu.tw (W.-H. Chiang).

https://doi.org/10.1016/j.ijbiomac.2024.135271
Received 22 June 2024; Received in revised form 23 August 2024; Accepted 31 August 2024
Available online 2 September 2024

(short circulation half-life of ca 105 min) and high affinity of ZA to bones (ca 55 % of intravenously-injected ZA) [24], the accumulation of ZA in extraskeletal tumors was significantly reduced, thus largely limiting clinical translation of ZA as a chemotherapy drug. To expand the utilization of ZA to treat extraskeletal tumors, a varied of nanoparticles such as liposomes [18,25,26], hybrid polymeric nanoparticles [20–22,27], nano-scaled metal-organic framework (nMOF) [13,28] have extensively developed as ZA vehicles to improve the pharmacokinetics and biodistribution of ZA. For example, Song's group designed a ZA-loaded liposome modified by a SA-octadecyl amine conjugate (ZA-SL) [18]. This ZA-SL can efficiently deliver ZA to TAMs by the combination of SA and Siglec-1 and show specific cytotoxicity or phenotypic remodeling of M2-like TAMs, thereby inhibiting tumor growth. Moreover, as reported by Li et al. [22], to reduce the premature leakage of ZA molecules, the anionic lipid-coated ZA-calcium nanocomplexes were encapsulated into poly(lactic-*co*-glycolic) acid (PLGA) nanoparticles stabilized with octadecanoic acid-hydrazone-polyethylene glycol (PEG). The in vivo studies demonstrated that the ZA-carrying PLGA nanoparticles effectively reduced the distribution of ZA in bones and promoted its deposition in tumors, thus significantly inhibiting the progress of orthotopically transplanted mammary tumors. Despite the effective inhibition of premature ZA leakage under a simulated physiological condition by the aforementioned nanoformulations [18,22], low ZA loading content (<6.5 wt%) and the lack of stimulus-triggered sufficient ZA release could largely restrict the anticancer effect of ZA molecules. To address these issues, Au and coworkers fabricated folate (FA)-targeted pH-responsive nMOF composed of a calcium (Ca)/ZA core and a PEG surface with a high ZA payload (76 wt%) [13]. The FA-targeted lipid coating facilitates the endocytosis of the nMOFs into FA-overexpressed cancer cells, allowing the nMOFs to accelerate the release of ZA in mildly acidic endosomes. Importantly, the in vivo antitumor activity studies in H460 and PC3 xenograft tumor-bearing mice demonstrated that the FA-targeted Ca/ZA nMOFs enhanced the direct antitumor potency of ZA molecules.

In the last decade, various organometallic nanoparticles have attracted much attention in biomedical fields and have been characterized to exhibit anticancer, antibacterial, antifungal, and antioxidant properties [29–33]. Moreover, some organometallic nanoparticles have been utilized as drug delivery systems [13,28,34]. Among them, various Fe-based nMOFs have been demonstrated to be applied in cancer chemodynamic therapy (CDT) by converting endogenous hydrogen peroxide (H_2O_2) into toxic hydroxyl radicals (•OH) upon intratumoral Fe^{3+}/Fe^{2+}-mediated Fenton or Fenton-like reactions, thereby eliciting oxidative damage to tumors [35–38]. Hyaluronic acid (HA), a natural polysaccharide, is composed of a simple repeating disaccharide of d-glucuronic acid and *N*-acetyl-d-glucosamine linked by β(1 → 3) linkages and shows good biocompatibility and biodegradability. HA has been verified to be a ligand of CD44 receptor overexpressed on numerous cancer cell membranes and extensively modified on the surfaces of various nanoparticles for active tumor-targeted drug delivery [37,39–41]. Considering the viewpoints mentioned above, in order to largely enhance the therapeutic efficacy of ZA molecules on breast tumors, it is required to design versatile nanoplatforms capable of effectively carrying ZA, controlling ZA release, and selectively delivering ZA to tumor sites. To this end, in this study, through the coating of HA segments on the surfaces of the ferric ion (Fe^{3+})-based MIL-88B nanobullets (MNs), a kind of nMOF, the HA-covered MNs (HMNs) were attained as ZA vehicles (Scheme 1a). The designed ZA-carrying HMNs (ZA@HMNs) were expected to realize CD44-overexpressed tumor-targeted ZA delivery and combine the ZA-mediated chemotherapy with HMNs-based CDT and ferroptosis for better treatment of breast cancer (Scheme 1b). The physicochemical characterization showed that the ZA@HMNs exhibited a high ZA payload (ca 29.6 wt%) and outstanding colloidal stability in a serum-containing milieu. Notably, through acidity/glutathione (GSH)-triggered disintegration of ZA@HMNs, the release of ZA and Fe^{3+} was remarkably accelerated. Also, the ZA@HMNs not only consumed GSH by GSH-mediated Fe^{3+} reduction but also efficiently converted H_2O_2 into •OH via Fenton or Fenton-like reaction in response to pH reduction from 7.4 to 5.0. After being internalized by 4T1 breast cancer cells upon CD44-mediated endocytosis, the ZA@HMNs

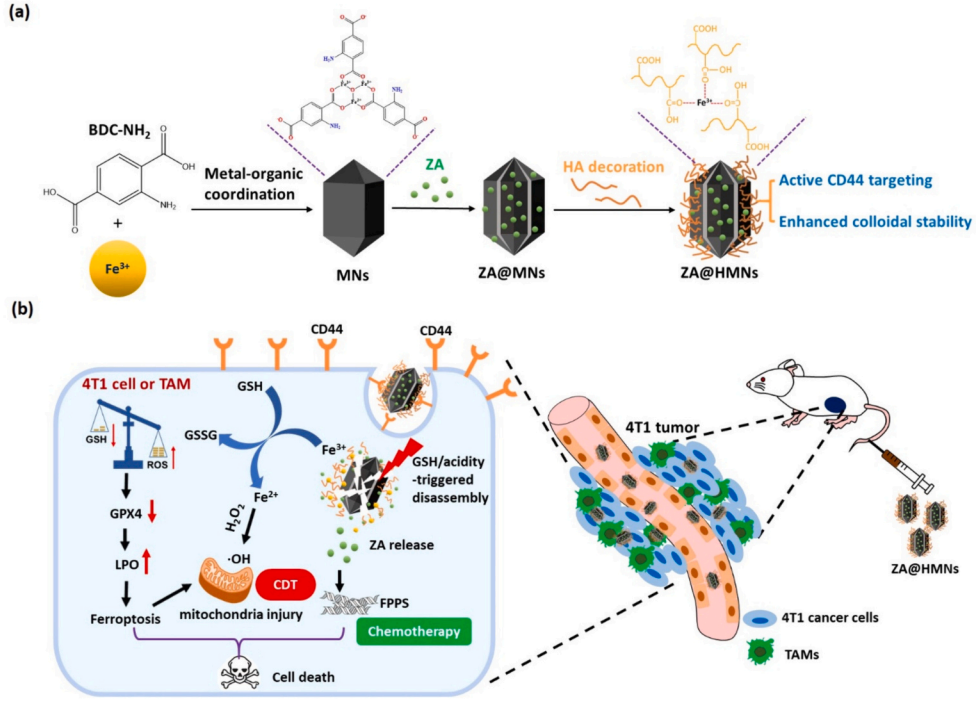

Scheme 1. Schematic illustration of ZA@HMNs for tumor treatment. (a) Synthetic approaches and coordination structures of ZA@HMNs. (b) The therapeutic mechanism of ZA@HMNs: disassembly of ZA@HMNs to release ZA and Fe^{3+}, Fe^{2+} generated from GSH-mediated Fe^{3+} reduction to convert H_2O_2 into •OH, •OH-elicited mitochondria damage, GSH depletion-elicited LPO, and ZA-mediated FPPS inhibition, thus leading to cell death.

depleted intracellular GSH via Fe^{3+}/Fe^{2+} redox process and degraded endogenous H_2O_2 into •OH, thus leading to lipid peroxidation (LPO) and mitochondria injury. Through the combination of ZA chemotherapy with HMNs-based CDT, the ZA@HMNs displayed sound cytotoxicity on 4T1 cells and macrophage-like RAW 264.7 cells. Importantly, the in vivo studies demonstrated that the CD44-targeting ZA@HMNs efficiently deposited in 4T1 tumor sites, thus hindering tumor growth via chemo/chemodynamic therapy as compared to free ZA chemotherapy alone and HMNs-mediated CDT. As a consequence, the ZA@HMNs developed in this work achieved the breast tumor-targeted effective delivery of chemo/chemodynamic therapy, providing a promising strategy for breast tumor treatment.

2. Materials and methods

2.1. Materials and cell lines

ZA was acquired from Tokyo Chemical Industry, CO., LTD (Japan). Anhydrous iron (III) chloride (97 %) was obtained from SHOWA (Japan). HA sodium salt (Mw = 30,000–50,000 g/mol or 3000–5000 g/mol, ≧91 %) was purchased from Glentham Life Science Ltd. (UK). 2-Aminoterephthalic acid (BDC-NH_2, 99 %) was attained from Alfa Acesar (USA). Propidium (PI, 94 %), methylene blue (MB) solution, dichloro-dihydro-fluorescein diacetate (DCFH-DA, ≧97 %) and RPMI-1640 medium were purchased from Sigma-Aldrich (USA). 2,2′-Azinobis(3-ethylbenzthiazoline-6-sulfonic acid) (ABTS, 95 %) was obtained from Combi-Blocks (USA). 1,10-phenanthroline monohydrate (Phe, ≥99.5 %) was attained from Thermo Fisher Scientific. Fetal bovine serum (FBS) was purchased from Hyclone (USA). Hoechst 33342 and BODIOY™ 581/591 C11 was obtained from (Invitrogen) (USA). JC-1 assay kit was purchased from MedChemExpress (USA). 5,5′-dithiobis (2-nitrobenzoic acid) (DTNB) was purchased from Fluorochem (UK). 3-(4,5-Dimethylthiazol-2-yl)-2,5-diphenyltetrazolium bromide (MTT, >98 %) was obtained from Alpha biochemistry (Taiwan). 3,3′,5,5′-Tetramethylbenzidine (TMB, 99 %) was purchased from Acros Organics (USA). Calcein-AM was obtained from AAT Bioquest (USA). Indocyanine green (ICG, 95.4 %) was obtained from Chem-Impex International, Inc. (USA). Anti-Ki67 antibodies (no. ab15580) and Anti-Glutathione peroxidase 4 (GPX4) antibodies (no. ab125066) were obtained from Abcam. Deionized water was produced from Milli-Q Synthesis (18 MΩ, Millipore). All other chemicals were reagent grade and used as received. 4T1 (murine breast cancer cell line), RAW 264.7 cells, and WS1 cells (human skin fibroblast cells) were obtained from the Food Industry Research and Development Institute (Hsinchu City, Taiwan).

2.2. Synthesis of MNs

The MNs used in this work were synthesized by a previously reported approach with minor modifications [42]. Briefly, $FeCl_3$ (8.9 mg) and BDC-NH_2 (17.8 mg) were dissolved in 5.0 mL ethanol, respectively. Afterward, the BDC-NH_2 solution was slowly added to the $FeCl_3$ solution and stirred at 40 °C for 1.5 h. The MNs were collected by centrifugation (35 °C, 16,000 rpm, 20 min) and washed triplicate with ethanol and once with deionized water. The attained MNs were dispersed in 1.5 mL deionized water and stored at 4 °C for further use.

2.3. Synthesis of ZA@HMNs

The ZA@HMNs were prepared according to the following methods. ZA (2.0 mg) was dissolved in deionized water, and the pH of ZA solution was adjusted to 8.0 with 1 M NaOH. Next, the ZA solution (1.0 mL, 2.0 mg/mL) was dropwise added into the as-synthesized MN solution (2.0 mL, 2 mg/mL) under an ice bath and stirred for 1 h. The resulting solution was dropped slowly in the aqueous solution of HA (Mw = 30,000–50,000 g/mol, 2.0 mL, 24 mg/mL) and further stirred for 24 h. The obtained ZA@HMNs were collected by centrifugation (16,000 rpm, 20 min) and washed triplicate with deionized water to remove unloaded ZA and residual HA segments. Finally, after being sonicated for 15 s, the ZA@HMNs were re-dispersed in 2.0 mL deionized water and stored at 4 °C for further use. For comparison, at a HA/MN weight ratio of 6.0 in feed, the HMNs were prepared in a similar approach. Moreover, to evaluate the effect of HA molecular weight on the colloidal stability of ZA@HMNs at a HA/MN weight ratio of 12.0 in feed, the ZA@HMNs were prepared by using short HA (Mw = 3000–5000 g/mol) instead of long HA (Mw = 30,000–50,000 g/mol).

2.4. Characterization

A D8 Discover X-ray diffractometer (Bruker, Germany) with CuKα radiation (40 kV, λ = 0.15 nm) was employed to attain the X-ray diffraction (XRD) patterns of MNs, HMNs, and ZA@HMNs. The morphology of various MNs was attained by transmission electron microscope (TEM) (JEM-1400 FLASH, JEOL, Japan) and scanning electron microscope (SEM) (JEOL JSM-7800F Prime Schottky Field Emission SEM, Japan). X-ray energy dispersive spectroscopy (EDS) elemental mapping of ZA@HMNs was attained with TEM (JEM-F200, JEOL). The particle size and size distribution of various MNs in aqueous solutions were determined by dynamic light scattering (DLS) using a Brookhaven BI-200SM goniometer equipped with a BI-9000 AT digital correlator using a solid-state laser (35 mW, λ = 637 nm) detected at a scattering angle of 90°. The zeta potential of MNs, HMNs, and ZA@HMNs in aqueous solutions was measured with a Litesizer 500 (Anton Paar, USA). At least triplicate measurements of each sample were conducted and then averaged. The chemical compositions of various MNs and HA segments were characterized by Fourier transform infrared (FT-IR) microscopy (FT-720, HORIBA, Japan). X-ray photoelectron spectroscopy (XPS) analysis of different MNs was performed by a PHI 5000 VersaProbe III X-ray photoelectron spectrometer (ULVAC-PHI, Japan) with AlKα radiation (hγ = 1486.6 eV) at 15 kV and 150 W.

2.5. Determination of Fe^{3+} and ZA content

To quantify the Fe^{3+} and ZA content of various MNs, a prescribed amount of the purified ZA@HMNs and HMNs were diluted 20 times with HNO_3 solution (1 %), and the mixture was then stirred for 24 h to ensure the complete dissolution of MNs. The Fe^{3+} and ZA concentration was determined by inductively coupled plasma-atomic emission spectrometry (ICP-AES) with an Agilent 725 emission spectrometer. The loading content (LC) of cargo was estimated by the following equation:

$$\text{LC of cargos (wt\%)} = (\text{weight of loaded cargo}/\text{total weight of cargo} - \text{loaded MNs}) \times 100\%.$$

2.6. In vitro ZA and Fe^{3+} dissolution test

For in vitro ZA release performance, the ZA@HMNs were dispersed in a pH 7.4 aqueous solution and pH 5.0 aqueous solution containing 10 mM GSH, respectively, and stirred at 37 °C. At the prescribed time intervals, the dispersion was centrifugated (16,000 rpm, 10 min) to collect the supernatant. The ZA concentration of the supernatant was analyzed by ICP-AES.

For the Fe^{3+} release study, the ZA@HMNs were dispersed in 10.0 mM GSH-containing aqueous solutions of pH 7.4 and 5.0, respectively, and stirred at 37 °C. 900 μL of dispersion was periodically withdrawn and mixed with 100 μL of Phe solution (0.2 mM). The mixture solution was equilibrated at 37 °C for 30 min for the formation of tangerine Fe^{2+}/Phe complexes. The absorbance of the resulting solution at 512 nm was measured. At least triplicate measurements of each sample were conducted and then averaged.

2.7. Fe^{2+} generation and GSH consumption

The Phe assay was utilized to confirm that Fe^{3+} ions of ZA@HMNs can be reduced to Fe^{2+} ions by GSH. In brief, ZA@HMNs (50 μg/mL) were dispersed in pH 7.4 PBS containing GSH (10 mM) and Phe (0.2 mM) and incubated at 37 °C for 2 h. Afterward, the resulting solution was centrifugated (16,000 rpm, 20 min) to remove the ZA@HMNs. The absorption spectrum of the supernatant was obtained by a UV/Vis spectrophotometer (U2900, HITACHI). For comparison, the experiment was also conducted using the following groups: ZA@HMNs in the lack of GSH, GSH alone, and $FeCl_3$ + GSH.

The GSH-depleting performance of ZA@HMNs was assessed by DTNB assay. Briefly, the ZA@HMNs (100 μg/mL) were dispersed in 100 μM GSH-containing pH 7.4 aqueous solution and incubated at 37 °C for 2, 4, 8, and 24 h. Next, at different time intervals, the solution was centrifugated (16,000 rpm, 10 min) to collect the supernatant. 900 μL of supernatant was added into 100 μL of 0.5 mM DTNB, and the reaction was carried out for 10 min. The UV/Vis spectrum of the resulting solution was measured with a UV/Vis spectrophotometer.

2.8. Catalytic performance

The catalytic performance (•OH production) of ZA@HMNs at pH 7.4 and 5.0 was explored by determining the absorption of oxTMB generated from the oxidation of TMB by •OH. Briefly, ZA@HMNs (50 μg/mL) were dispersed in aqueous solutions of pH 7.4 and 5.0 containing 100 μM H_2O_2 and 0.5 mM TMB and then incubated in dark at 37 °C for 2 h. The resulting solutions were centrifugated (12,000 rpm, 10 min) to collect the supernatant. The UV/Vis spectrum of the supernatant was attained by a UV/Vis spectrophotometer. Moreover, the ABTS assay was used to evaluate the •OH generation of ZA@HMNs. ZA@HMNs (50 μg/mL) were dispersed in aqueous solutions of pH 7.4 and 5.0 containing 100 μM H_2O_2 and 0.5 mM ABTS and then incubated in dark at 37 °C for 2 h. The resulting solutions were centrifugated (12,000 rpm, 10 min) to collect supernatant. The UV/Vis spectrum of the supernatant was attained by a UV/Vis spectrophotometer. The UV/Vis spectra of the resulting solutions were determined by a UV/Vis spectrophotometer. On the other hand, the MB assay was employed to investigate the effects of GSH addition on the •OH generation of ZA@HMNs via Fenton or Fenton-like reaction. ZA@HMNs (50 μg/mL) were dispersed in aqueous solutions of pH 7.4 containing 100 μM H_2O_2, 0.05 mM MB and GSH (2 or 10 mM) and then incubated in dark at 37 °C. At the prescribed time intervals, the dispersion was centrifugated (10,000 rpm, 5 min) to collect supernatant. The absorbance of the supernatant at 664 nm was determined by a UV/Vis spectrophotometer. The MB absorbance measured at different time intervals was normalized to that at the beginning.

2.9. ICG labeling of ZA@HMNs

To study the in vitro cellular internalization and in vivo biodistribution of ZA@HMNs by fluorescence imaging, the amphiphilic fluorescent dye, ICG, was encapsulated into these nanoparticles by the following approach. In brief, the ZA solution (1.0 mL, 2.0 mg/mL) and ICG-containing ethanol (1 mL, 0.4 mg/mL) were dropwise added into the as-synthesized MN solution (2.0 mL, 2 mg/mL) under ice bath and stirred for 1 h. The resulting solution was dropped slowly in aqueous solution of HA (2.0 mL, 24 mg/mL) and further stirred for 24 h. The obtained ZA@HMNs were collected by centrifugation (16,000 rpm, 20 min) and washed triplicate with deionized water to remove unloaded ZA and ICG. Finally, after being sonicated for 15 s, the ICG-labeled ZA@HMNs were re-dispersed in 2.0 mL deionized water and stored at 4 °C.

2.10. In vitro cellular uptake

The internalization of ICG-labeled ZA@HMNs by 4T1 cells at 37 °C was evaluated by the FACSCalibur flow cytometer (BD Bioscience). 4T1 cells (2×10^5 cells/well) seeded in 6-well plates were incubated with free ICG molecules as the control and ZA@HMNs with or without free HA addition (ICG concentration = 5 μM, HA concentration = 20 mg/mL), respectively, at 37 °C for 1 h. Next, after being detached with trypsin-EDTA solution, the treated 4T1 cells were dispersed in PBS (0.6 mL) and centrifugated (1500 rpm, 5 min) to collect cell pallets. The cell pellet was re-suspended in PBS (0.1 mL), and the fluorescence intensity of a minimum of 1×10^4 cells was analyzed.

On the other hand, the CD44-mediated cellular uptake of ICG-labeled ZA@HMNs by 4T1 cells was observed by fluorescence imaging. 4T1 cells (2×10^5 cells/well) seeded onto 22 mm round glass coverslips in 6-well plates were incubated with ICG-labeled ZA@HMNs (ICG concentration = 5 μM) in the presence or absence of free HA segments (20 mg/mL) at 37 °C for 1 h. After being rinsed triplicate with HBSS and immobilized with 4 % formaldehyde, the cell nuclei were stained with Hoechst 33342 for 5 min. The cellular images were obtained with a confocal laser scanning microscope (CLSM) (Olympus, Fluo View FV3000, Japan) equipped with a Hoechst set (Ex. 405 nm) and an ICG set (Ex. 640 nm).

2.11. Intracellular GSH depletion and •OH production

To assess intracellular GSH consumption of ZA@HMNs, 4T1 cells (2×10^5/well) seeded in a 6-well plate were incubated with ZA@HMNs of various concentrations (50, 100, and 200 μg/mL), respectively, at 37 °C for 24 h. After being rinsed twice with PBS, the treated cells were detached with trypsin-EDTA and then centrifugated (1500 rpm) for 5.5 min. Next, the cell pellet was re-dispersed in 0.3 mL RIPA buffer, followed by freezing at -20 °C and thawing for cell lysis. After being centrifuged (16,000 rpm for 10 min), 100 μL of supernatant was taken out and mixed with 50 μL DTNB (50 μM). The reaction was carried out for 20 min. Finally, the absorbance of DTNB in the resulting solution was measured by a microplate reader at a wavelength of 405 nm. At least triplicate measurements of each sample were conducted and then averaged. The intracellular GSH level was calculated by the following formula:

$$\text{Intracellular GSH level } (\%) = \frac{Absorbance\ of\ experimental\ group}{Absorbance\ of\ control\ group} \times 100$$

On the other hand, to confirm the intracellular •OH generation, 4T1 cells (2×10^5 cells/well) seeded onto 22 mm round glass coverslips in 6-well plates were incubated with ZA@HMNs at pH 6.5 in the presence of 100 μM H_2O_2 (mimic tumor microenvironment) or pH 7.4 without H_2O_2 at 37 °C for 24 h. After removing the culture medium, the cells were incubated with DCFH-DA (10 μM) for 30 min and washed triplicate with HBSS, followed by immobilization with 4 % formaldehyde. The cellular images were acquired using CLSM (Olympus, FluoView FV3000, Japan) at excitation wavelengths of 485 nm for DCF.

2.12. Intracellular LPO determination

4T1 cells (2×10^5/well) attached in a 6-well plate were incubated with free ZA molecules (100 μM), HMNs (200 μg/mL), and ZA@HMNs (ZA concentration = 100 μM; HMN concentration = 200 μg/mL), respectively, in the presence of H_2O_2 (100 μM) at 37 °C for 24 h. After removing the culture medium, the cells were treated with BODIPY™ 581/591 C11 (5 μM) for 30 min and rinsed with HBSS, followed by immobilization with 4 % formaldehyde for 15 min. The intracellular LPO was observed by fluorescence microscopy (ZEISS Axio Imager M2) at excitation wavelengths of 514 nm for BODIPY.

2.13. Mitochondrial membrane potential (MMP) analysis

The MMP detection kit (JC-1) was adopted to observe the depolarization of the mitochondria membranes. 4T1 cells (2×10^5/well) attached in a 6-well plate were incubated with free ZA molecules (100

μM), HMNs (200 μg/mL), and ZA@HMNs (ZA concentration = 100 μM; HMN concentration = 200 μg/mL), respectively, in the presence of H_2O_2 (100 μM) at 37 °C for 24 h. After discarding the culture medium, the cells were treated with JC-1 (2 μM) for 30 min and rinsed triplicate with HBSS, followed by immobilization with 4 % formaldehyde. The cellular images were attained by fluorescence microscopy (ZEISS Axio Imager M2) at 485 and 535 nm excitation wavelengths for JC-1 monomer and JC-1 aggregate, respectively.

2.14. In vitro anticancer effect of chemo/chemodynamic therapy

Free ZA molecules, HMNs, and ZA@HMNs were dispersed in 100 μM H_2O_2-containing RPMI-1640 medium, respectively. 4T1 cells (1×10^4 cells/well) attached in a 96-well plate were incubated in RPMI-1640 containing 10 % FBS and 1 % penicillin at 37 °C for 24 h. The spent medium was then replaced with 120 μL of the above formulations and further incubated for an additional 48 h. Afterward, after removing the culture medium, 100 μL of MTT (0.25 mg/mL) was added into each well, followed by incubation at 37 °C for 3 h. After eliminating the suspension, 120 μL of DMSO was added into each well to completely dissolve the precipitate, and the absorbance at 570 nm was determined by a microplate reader (BioTek 800 TS). On the other hand, the viability of RAW264.7 cells treated with different formulations for 24 h was evaluated in a similar manner. Furthermore, to explore the effect of HMNs on normal cells, the viability of WS1 cells incubated with HMNs at 37 °C for 48 h was assessed by MTT assay.

The anticancer effect of chemo/chemodynamic therapy delivered by ZA@HMNs on 4T1 cells was further evaluated by calcein-AM/PI staining of live/dead cells. 4T1 cells (1.5×10^5 cells/well) attached in a 12-well plate were incubated with free ZA molecules (100 μM), HMNs (200 μg/mL), and ZA@HMNs (ZA concentration = 100 μM; HMN concentration = 200 μg/mL), respectively, in the presence of 100 μM H_2O_2 for 24 h. After being rinsed with HBSS, the cells were stained with calcein-AM (800 μL, 0.2 μM) for 45 min, followed by staining with PI (800 μL, 25 μg/mL) for 30 min. The cellular images were attained with a NIB-100F inverted fluorescent biological microscope.

2.15. Animals and tumor model

Female BALB/c mice (6–7 weeks old) were purchased from the National Laboratory Animal Center (Taiwan) and cared according to the Guidance Suggestions for the Care and Use of Laboratory Animals, approved by the Administrative Committee on Animal Research in the Chung Shan Medical University (Taiwan) (IACUC Approval No: 2722). To establish a tumor model, 100 μL of PBS containing 2×10^6 4T1 cells was subcutaneously injected into the right thigh of mice. Tumor volume (V) was calculated as follows: $V = L \times W^2/2$, where W is the tumor dimension at the widest point and L is the tumor dimension at the longest point.

2.16. In vivo imaging and biodistribution

When the tumor volume reached 80–120 mm^3, mice were randomly assigned into 3 groups ($n = 3$) and intravenously injected with PBS, free ICG molecules, and ICG-labeled ZA@HMNs (150 μL), respectively, at a dosage of 1.6 mg/kg ICG. The fluorescence signals of ICG (Ex. 710 nm and Em. 760 nm) at 2, 4, and 24 h post-injection were collected by an IVIS imaging system (IVIS Lumina II, Caliper, LifeSciences, MA, USA). The treated mice were sacrificed by CO_2 euthanasia at 24 h post-injection, and the major organs and tumors were collected for imaging by IVIS.

2.17. In vivo tumor growth suppression

While the tumor volume of mice approached 80–120 mm^3, mice were randomly assigned into 4 groups ($n = 4$ per group): (i) PBS; (ii) free ZA molecules; (iii) HMNs; (iv) ZA@HMNs. Mice in different groups were intravenously injected with the corresponding reagents (150 μL) at a dosage of 0.8 mg ZA/kg and/or a dosage of 5 mg HMNs/kg. Each group was treated with a total of two doses on days 0 and 2. The tumor volume and body weight of different groups were measured every two days until 14 days post-treatment. To evaluate the antitumor efficacy, the relative tumor volumes (V/V_o) of different groups were also attained by the normalization of the final tumor volumes (V) against the initial tumor volumes (V_o). Afterward, all mice were euthanized, and the major organs, including the heart, liver, spleen, lung, and kidney, and tumors were harvested. Then, the tumors were photographed and weighed. Tumor sections of pertinent size were stained with hematoxylin and eosin (H&E), anti-Ki67 antibodies, and anti-GPX4 antibodies, respectively, and observed by digital microscope. Moreover, sections of major organs were stained with H&E and observed by the same instrument.

2.18. Statistical analysis

The data are presented as mean ± standard deviation. One-way or two-way ANOVA analysis was used to determine the differences among the groups. ns > 0.05, $^*p < 0.05$, $^{**}p < 0.01$, $^{***}p < 0.001$. All statistical analyses were performed using Prism software (PRISM 5.01 GraphPad Software).

3. Results and discussion

3.1. Synthesis and characterization of ZA@HMNs

The detailed synthetic approach of ZA@HMNs is presented in Scheme 1a. The MNs from the coordination of BDC-NH_2 ligands with $FeCl_3$ molecules were initially synthesized by a simple and economical method instead of the traditional hydrothermal methods [42]. The XRD pattern of MNs revealed the well-developed crystalline with diffraction peaks at 9.2 and 10.4°, similar to those previously reported for other MIL-88B nMOF [42,43], thus confirming the successful synthesis of organic-Fe framework (Fig. 1a). The attained MNs were characterized by SEM to exhibit octahedral shape with a dimension of approximately 190 ± 16 nm in length and 70 ± 6 nm in width (Fig. 1b). The spindle-like shape of MNs was also observed in their TEM images. Moreover, the MNs dispersed in deionized water displayed a uniform size distribution of ca. 126.8 nm (Fig. 1c). However, after being dispersed in 10 % FBS-containing RPMI medium at 37 °C mimicking physiological condition, the MNs showed considerably enlarged particle size (beyond 1000 nm) over time (Fig. S1a and b), being indicative of the occurrence of inter-particle aggregation. Such a severe inter-particle clumping of MNs is not favorable for the application of tumor-targeted drug delivery. To improve the colloidal stability of MNs in a physiological environment and endow MNs with active tumor-targeting ability, HA segments capable of specific targeting CD44-overexpressed cancer cells were coated on the surfaces of MNs through their coordination with ferric ions (Scheme 1a) [44,45]. In this work, two different weight ratios of HA segments to MNs (6:1 or 12:1) in feed were used in the preparation of HMNs. As shown in Fig. 1d, in addition to the characteristic absorption bands of C—N stretching vibration of the benzene ring and the out-of-plane bending vibration of the C—H bond at 1251 cm^{-1} and 761 cm^{-1}, respectively, and that of Fe-O-Fe tensile vibration at 531 cm^{-1} from MNs, the absorption band of C—O stretching vibration in the saccharide structure of HA at ~1100 cm^{-1} was observed in the FT-IR spectrum of HMNs (HA/MN (*w*/w) = 12), suggesting the successful decoration of HA segments on the surfaces of MNs. Furthermore, different from MNs with positive zeta potential (ca +18 mV), the HMNs with different HA/MN weight ratios possessed appreciably negative values of zeta potential (ca −30 mV) due to surface covering of carboxylic acid-rich HA segments (Fig. 1e). Also, the particle size (ca 148.7 nm) of HMNs (HA/MN (w/w) = 12) was somewhat larger than that (126.8 nm) of MNs due to the presence of HA-constituted coating layer

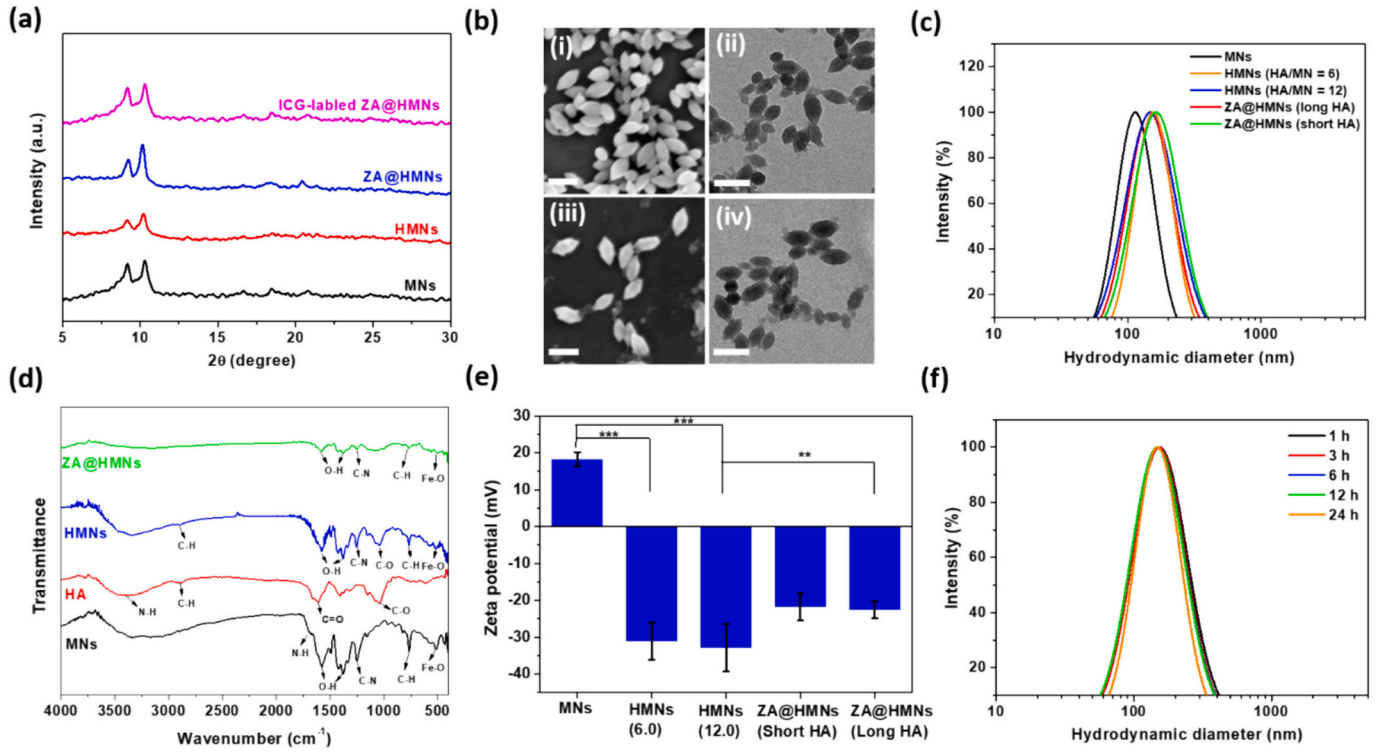

Fig. 1. (a) XRD patterns of MNs, HMNs, ZA@HMNs, and ICG-labeled ZA@HMNs. (b) SEM images of (i) MNs and (iii) HMNs. TEM images of (ii) MNs and (iv) HMNs. Scale bars are 200 nm. (c) DLS particle size distribution profiles of MNs in deionized water, HMNs, and ZA@HMNs in pH 7.4 0.15 M PBS. (d) FT-IR spectra of MNs, HA, HMNs, and ZA@HMNs. (e) Zeta potential of MNs, HMNs, and ZA@HMNs dispersed in pH 7.4 aqueous solutions ($n = 3$). (f) DLS particle size distribution profiles of HMNs (HA/MN (w/w) = 12) in 10 % FBS-containing RPMI culture medium for different time intervals. ns > 0.05, *$p < 0.05$, **$p < 0.01$, ***$p < 0.001$.

(Fig. 1c and Table 1). Note that the MNs with HA modification maintained the intact crystalline structure and octahedral shape, as revealed in the XRD, SEM, and TEM characterization (Fig. 1a and b). Furthermore, based on the thermogravimetric profiles of HMNs (HA/MN (w/w) = 12) (Fig. S2), the HMNs were composed of ca 59.1 wt% MNs and 40.9 wt% HA segments. Importantly, different from the remarkably enlarged particle size of HMNs (HA/MN (w/w) = 6) in 10 % FBS-containing RPMI for 3 h due to severe inter-particle flocculation (Fig. S3), the virtually unchanged particle size of HMNs (HA/MN (w/w) = 12) under the same condition for 24 h was attained (Fig. 1f). The signifies that the adequate amount of hydrophilic HA segments covering the surfaces of HMNs plays a key role in enhancing their colloidal stability to avoid inter-particle aggregation. Therefore, the HMNs fabricated at a HA/MN weight ratio of 12 in feed were selected as ZA vehicles owing to their outstanding colloidal stability beneficial for tumor-targeted drug delivery via the enhanced permeability and retention (EPR) effect and HA-mediated CD44 targeting.

Through the chelation of ferric ions from MNs with phosphonate-bearing ZA molecules, followed by HA surface modification, the ZA@HMNs were obtained. As presented in Fig. 2a, compared to the XPS spectrum of MNs with or without HA decoration, the XPS spectrum of ZA@HMNs showed an extra characteristic peak of P 2p at 145.8 eV, proving successful encapsulation of phosphonate-containing ZA molecules into HMNs. Moreover, two binding energy peaks at 710.0 eV corresponding to the Fe $2p_{3/2}$ main peak and 724.0 eV ascribed to the Fe $2p_{1/2}$ main peak were observed in the Fe 2p XPS spectrum of ZA@HMNs (Fig. S4), illustrating the presence of Fe^{3+} ions within ZA@HMNs. Note that the XRD pattern of ZA@HMNs was comparable to that of HMNs, illustrating that the ZA@HMNs retained intact crystalline structure. Also, as shown in TEM and SEM images (Fig. 2b), the ZA@HMNs exhibited a bullet-like shape similar to HMNs and MNs. The ZA loading content was determined by ICP-AES to be 29.6 wt% (Table 1) and ZA molecules were evenly distributed in the ZA@HMNs as evidenced by homogeneous distribution of N, P, O and Fe elements in the EDS mappings (Fig. 2c). Importantly, the slightly increased particle size and nearly unchanged size distribution of ZA@HMNs dispersed in 10 % FBS-containing RPMI for 24 h suggest their sound colloidal dispersion and robust structural stability (Fig. 2d). On the other hand, in order to investigate the effects of HA chain length on the dispersion stability of ZA@HMNs in the serum-containing milieu, at a fixed HA/MN weight ratio of 12, the short HA segments (Mw = 3–5 kDa) stead of long HA (Mw = 30–50 kDa) were used in the preparation of ZA@HMNs. In addition to the octahedral form (Fig. S5), the particle size of ZA@HMNs with short HA modification dispersed in pH 7.4 PBS was comparable to the counterparts with long HA decoration (Fig. 1c). However, the ZA@HMNs (short HA decoration) tended to aggregate into large particles in the 10 % FBS-containing RPMI medium (Fig. 2e). Apparently, compared to short HA segments, the long HA segments used as surface coating layers largely promoted the dispersion stability of ZA@HMNs. Due to their robust structural stability, a critical prerequisite for tumor-targeted chemo/chemodynamic therapy, the ZA@HMNs with modification of long HA segments were utilized for the following investigation.

As shown in Fig. 2f, with the solution pH being adjusted from 7.4 to 5.0, the particle size of ZA@HMNs was considerably enlarged beyond 1000 nm. Also, the massive aggregation and some disintegration of ZA@HMNs treated at pH 5.0 were observed in their TEM images

Table 1
DLS data and drug loading characteristics of HMNs and ZA@HMNs.

	Mean hydrodynamic diameter (nm)	PDI	LC	
			ZA	Fe^{3+}
HMNs	148.7 ± 4.46	0.17 ± 0.04	–	10.5 ± 2.8
ZA@HMNs	148.3 ± 4.66	0.16 ± 0.01	29.6 ± 3.9	17.6 ± 2.6

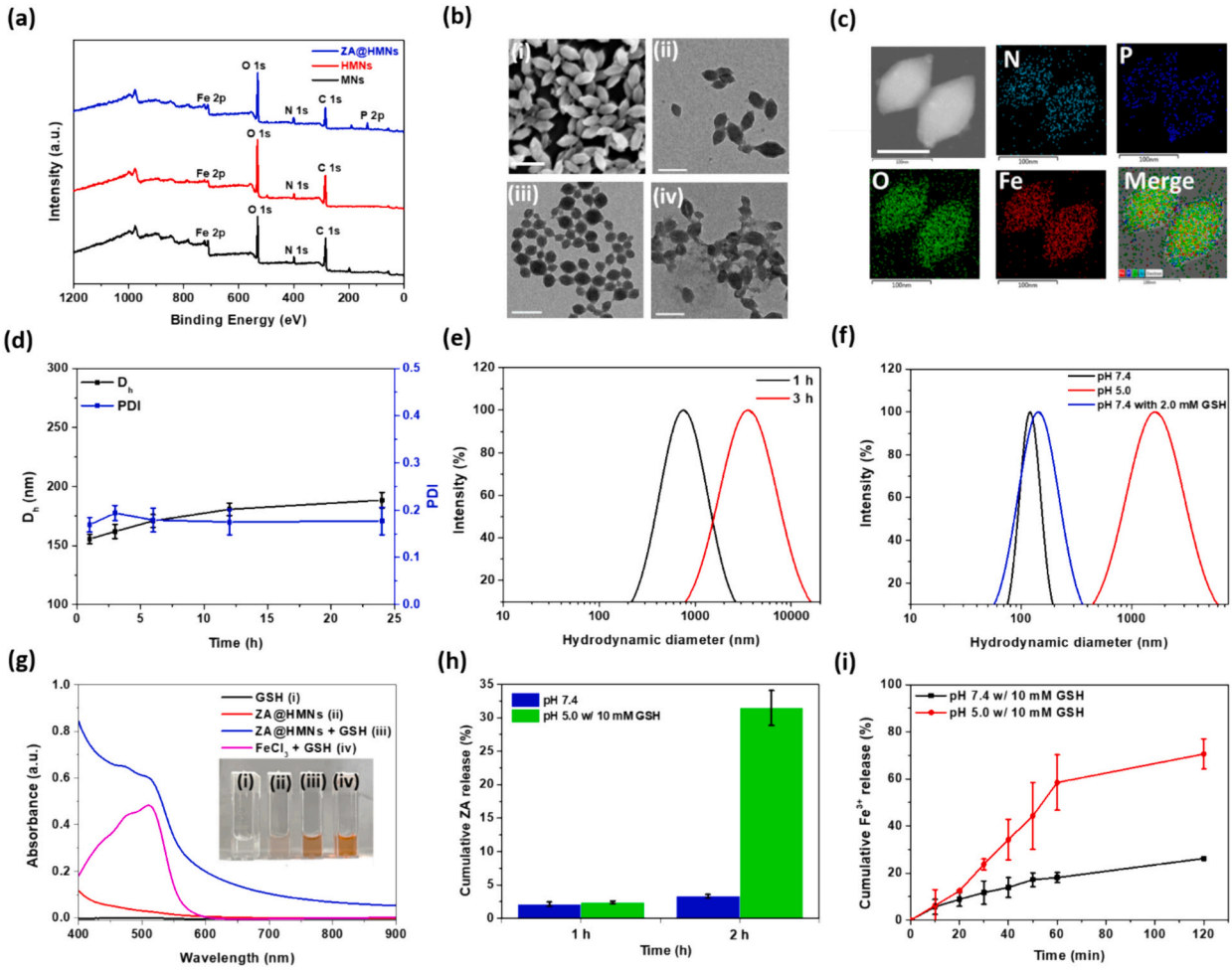

Fig. 2. (a) XPS spectra of MNs, HMNs, and ZA@HMNs. (b) SEM images of (i) pristine ZA@HMNs. TEM images of (ii) pristine ZA@HMNs and ZA@HMNs pretreated with (iii) GSH-containing pH 7.4 solution and (iv) GSH-containing pH 5.0 solution, respectively. Scale bars are 200 nm. (c) Corresponding element N, P, O, and Fe mapping images of ZA@HMNs. Scale bar was 100 nm. (d) Colloidal stability of ZA@HMNs (long HA modification) dispersed in 10 % FBS-containing RPMI culture medium ($n = 3$). (e) DLS particle size distribution profiles of ZA@HMNs (short HA decoration) dispersed in 10 % FBS-containing RPMI culture medium for 1 and 3 h. (f) DLS particle size distribution profiles of ZA@HMNs dispersed in aqueous solutions of pH 7.4 with or without 2.0 mM GSH and pH 5.0, respectively, for 24 h. (g) UV/Vis spectra of Phe receiving different treatments. Inset: photographs of the corresponding samples. (h) Cumulative ZA release of ZA@HMNs in pH 7.4 solution and 10.0 mM GSH-containing pH 5.0 solution, respectively, at 37 °C (n = 3). (i) Cumulative Fe^{3+} release profiles of ZA@HMNs in GSH-containing aqueous solutions of pH 7.4 and 5.0, respectively, at 37 °C (n = 3).

(Fig. S6). The findings could be attributed to the acidity-elicited decrease in the dissociation degree of carboxylic acid residues from HA-constituted surfaces leading to inter-particle aggregation of ZA@HMNs without electrostatic repulsion force. Furthermore, some studies reported that the acidity-enhanced protonation of carboxylic acid groups from BDC-NH_2 disrupted the coordination between Fe^{3+} ions and BDC-NH_2 ligands, thereby causing the Fe-based MOFs to be unstable in an acidic environment [37,46,47]. Next, Phe, a chelator with a high affinity for divalent metal ions, was used to confirm the generation of Fe^{2+} ions from ZA@HMNs in the presence of GSH. The catalytic efficiency of Fe^{2+} ions has been demonstrated to be higher than that of Fe^{3+} ions in the H_2O_2-involved Fenton reaction. As presented in Fig. 2g, after being mixed with 0.2 mM Phe and 2.0 mM GSH, the ZA@HMNs solution showed an obvious absorption peak at 525 nm and an appreciably red color, being similar to $FeCl_3$ receiving the same treatment. By contrast, in the lack of GSH, no significant absorption peak was attained for the aqueous solution containing ZA@HMNs and Phe. This demonstrates that the Fe^{3+} ions of ZA@HMNs can be reduced to Fe^{2+} ions by GSH, thus forming a tangerine complex with Phe. Notably, at pH 5.0 and in the presence of 2.0 mM GSH, the bullet-like shape of ZA@HMNs was dramatically disintegrated as revealed in their TEM images (Fig. 2b). Obviously, through GSH-mediated Fe^{3+} reduction and acidity-triggered cleavage of coordination bonds of Fe^{2+}/Fe^{3+} ions and BDC-NH_2 ligands, the structure of ZA@HMNs was remarkably destroyed. In contrast, the ZA@HMNs dispersed in a GSH-containing aqueous solution of pH 7.4 only exhibited somewhat increased particle size (Fig. 2f) but displayed a change in morphology from fusiform to spherical-like structure (Fig. 2b). This indicates that the formation of Fe^{2+} ions driven by the GSH-induced Fe^{3+} reduction could lead to rearrangement of some coordination bonds between Fe^{2+}/Fe^{3+} ions and BDC-NH_2 ligands, thus eliciting structure conversion of ZA@HMNs. Importantly, in the presence of 10.0 mM GSH, the cumulative release of Fe^{3+} and ZA payloads from ZA@HMNs was remarkably increased in response to pH reduction from 7.4 to 5.0 (Fig. 2h and i), illustrating that the structural collapse of ZA@HMNs could accelerate cargo liberation. In view of the previously reported quite low concentration of GSH in plasma (2–20 μM) and the intracellular acidic and GSH-rich environment (1–10 mM) [48], the acidity/GSH-responsive structural conversion and cargo liberation of ZA@HMNs were expected to decrease premature leakage of ZA and iron ions during blood circulation and promote their intracellular release for effective cancer treatment.

3.2. GSH depletion and ROS generation

In light of the above findings that the Fe^{3+} of ZA@HMNs interacts with GSH in a redox process to produce Fe^{2+} and glutathione disulfide (GSSG), as presented in Fig. 3a, the GSH-depleting capability of ZA@HMNs was further evaluated by DTNB assay [49]. As presented in Fig. 3b, the GSH alone as an important control group displayed a visibly characteristic peak at 412 nm, whereas the ZA@HMNs + GSH group showed appreciably reduced absorbance at 412 nm during 24 h, suggesting that ZA@HMNs consistently exhausted GSH by GSH-mediated Fe^{3+} reduction over time. Such a sustained GSH exhaustion of ZA@HMNs was expected to diminish the intracellular GSH-mediated •OH scavenging. Next, the •OH-generating capability of ZA@HMNs upon the Fenton reaction was evaluated by using TMB as a probe, which can be oxidized to oxTMB by •OH. The resulting oxTMB shows characteristic absorption at 650 nm. In the absence of H_2O_2, the ZA@HMNs-containing aqueous solutions at pH 7.4 or 5.0 have no significant absorption at 650 nm (Fig. 3c). Notably, in the presence of H_2O_2 (100 μM), the absorbance of oxTMB in aqueous solutions of ZA@HMNs at pH 5.0 was markedly increased compared to that at pH 7.4. Furthermore, the ABTS was further employed as a probe to detect •OH. The absorption of oxABTS from 400 to 800 nm in aqueous solutions of ZA@HMNs was significantly enhanced in response to pH reduction from 7.4 to 5.0 in the presence of H_2O_2 (100 μM), as observed in Fig. 3d. All of the aforementioned results demonstrate that the ZA@HMNs effectively converted H_2O_2 into •OH through the acidity-activated Fenton reaction, thus oxidizing TMB and ABTS (Fig. 3a). Similar findings regarding the acidity-enhanced Fenton reaction of MOF-based nanozymes were also reported elsewhere [50–52]. As mentioned earlier, the production of Fe^{2+} from GSH-mediated Fe^{3+} reduction of ZA@HMNs was assumed to promote the generation of •OH through the Fenton reaction. Therefore, the effect of GSH addition on the •OH generation performance of ZA@HMNs was further investigated by MB assay. Note that the absorbance of MB in ZA@HMN solution containing 100 μM H_2O_2 was remarkably decreased in the presence of GSH (Fig. 3e). When the GSH concentration was increased from 2 to 10 mM, the normalized absorbance of MB in ZA@HMN solution was appreciably reduced with time (Fig. 3f). Undoubtedly, the GSH-mediated Fe^{2+} generation of ZA@HMNs efficiently catalyzed H_2O_2 into •OH, thus enhancing MB degradation. According to the results, the created ZA@HMNs display the ability to deplete GSH and exhibit enhanced Fenton reaction activity under acidic and GSH-rich conditions similar to the intracellular environment of cancer cells, thereby being expected to enhance the anticancer effectiveness of CDT.

3.3. In vitro cellular uptake, intracellular GSH consumption, and •OH production

Several studies show that the HA-decorated therapeutic nanoparticles can actively target CD44-overexpressed cancer cells, thus promoting intracellular drug delivery [37,39–41]. Therefore, it was essential to evaluate the CD44-targeting capability of ZA@HMNs by in vitro cellular uptake study. Due to the lack of fluorescence property of ZA@HMNs, the amphiphilic fluorescence dye, ICG, was encapsulated into ZA@HMNs. As presented in Fig. S7, the ICG-labeled ZA@HMNs showed an appreciable red shift of feature absorption peak of ICG compared to free ICG molecules, indicating successful incorporation of ICG molecules into ZA@HMNs through π-π stacking of ICG with BDC-NH_2 in combination with the coordination between ICG and Fe^{3+}. The ICG loading content of ICG-labeled ZA@HMNs was determined to be ca 6.5 wt%. Moreover, the mean particle size of ICG-labeled ZA@HMNs was attained by DLS to be 146.2 nm (Fig. S8), being similar to that of ZA@HMNs. Next, the cellular internalization of ICG-labeled ZA@HMNs by CD44-overexpressed 4T1 cells was observed with flow cytometry and CLSM. Notably, with 1-h incubation, 4T1 cells incubated with ICG-labeled ZA@HMNs showed stronger ICG fluorescence signals in comparison with cells receiving both of the counterparts and free HA segments (Fig. 4a). Also, as shown in the CLSM images (Fig. 4b), the uptake of ICG-labeled ZA@HMNs by 4T1 cells pretreated with free HA segments was hindered, as reflected by the somewhat declined ICG fluorescence

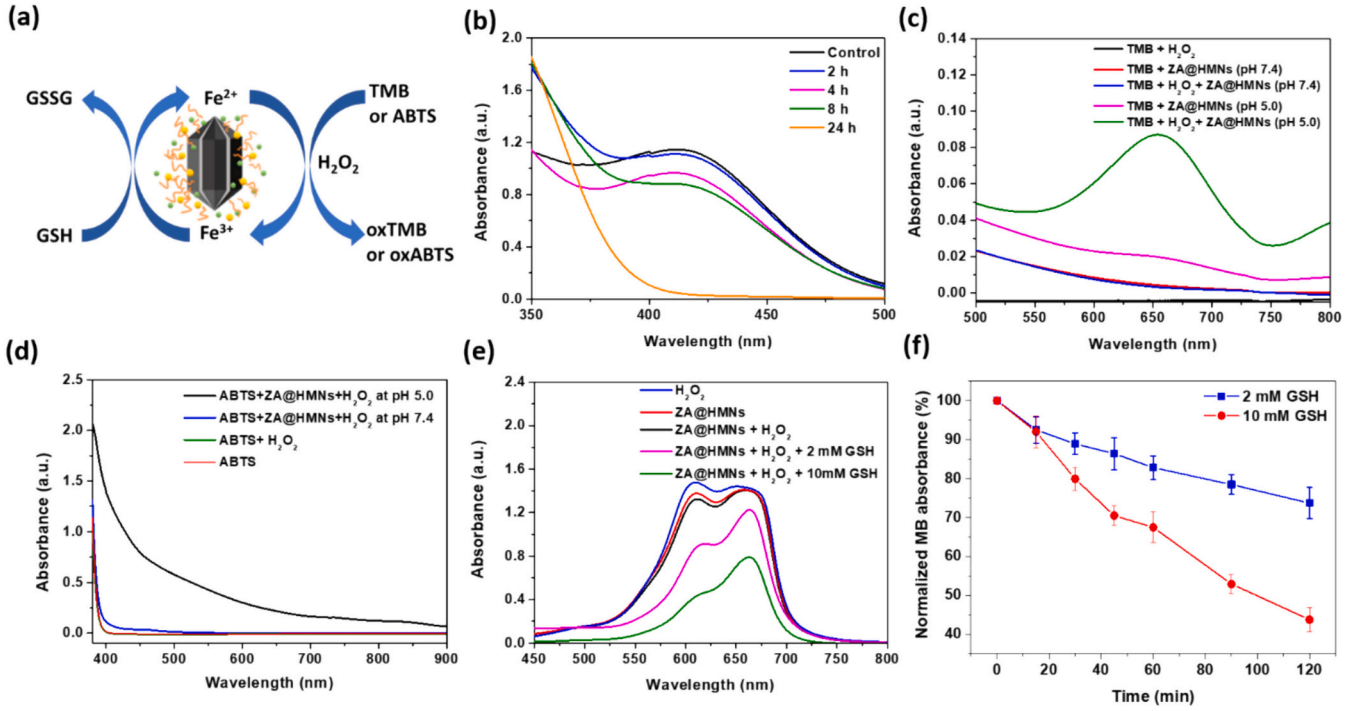

Fig. 3. (a) Schematic illustration of GSH depletion and •OH production of ZA@HMNs. (b) UV/Vis spectra of DTNB molecules dissolved in GSH solution pretreated with ZA@HMNs for different time intervals. UV/Vis spectra of (c) TMB molecules, (d) ABTS molecules, and (e) MB molecules receiving different treatments for 2 h. (f) Time-evolved normalized absorbance of MB molecules in aqueous solutions of ZA@HMNs containing 100 μM H_2O_2 and GSH (2 or 10 mM) ($n = 3$).

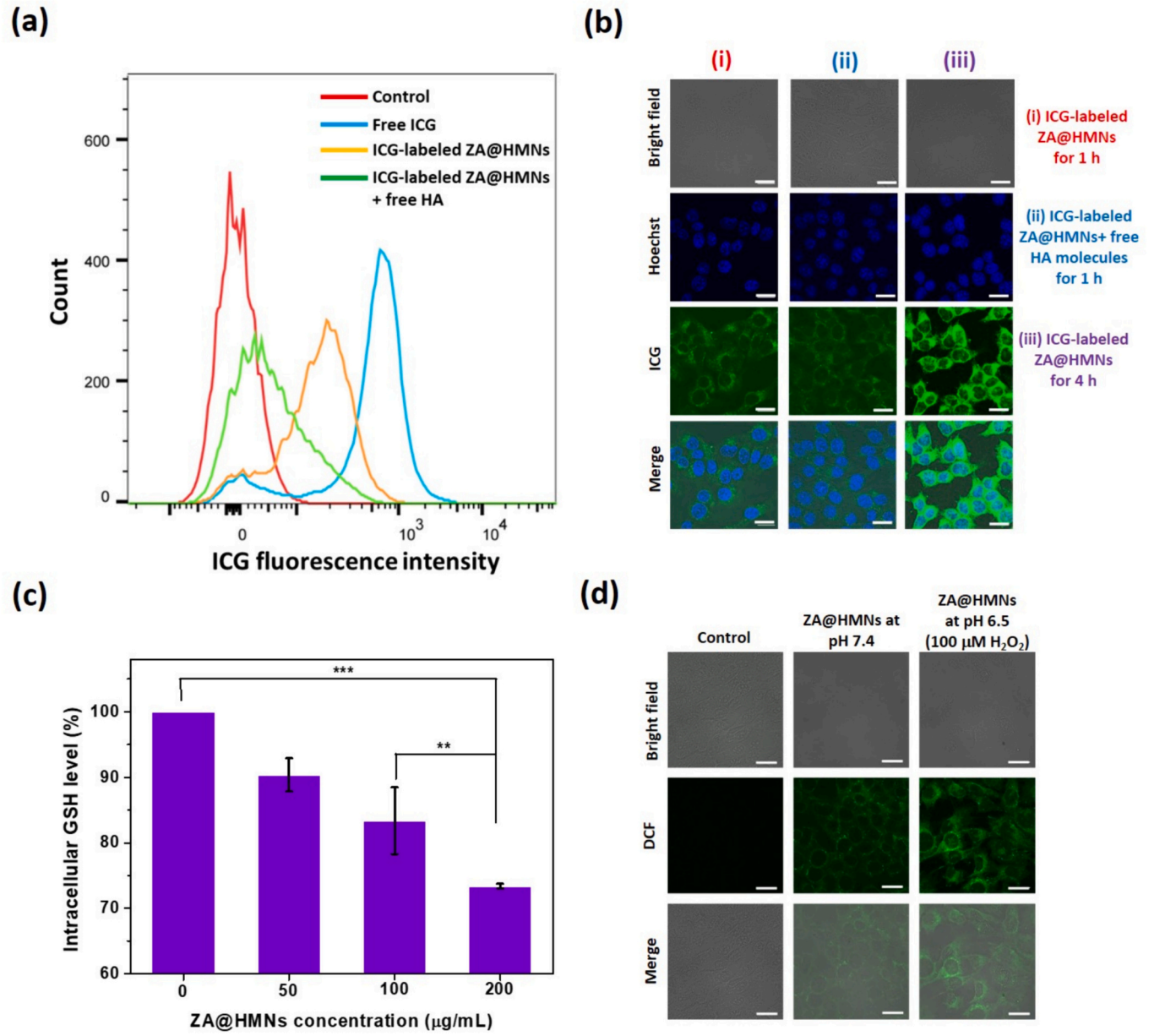

Fig. 4. (a) Flow cytometric histograms of 4T1 cells incubated with free ICG molecules or ICG-labeled ZA@HMNs in the presence or absence of free HA segments at 37 °C for 1 h. (b) CLSM images of 4T1 cells incubated with ICG-labeled ZA@HMNs and free HA segments for 1 h or ICG-labeled ZA@HMNs for 1 and 4 h at 37 °C. Scale bars are 20 μm. (c) Intracellular GSH level of 4T1 cells receiving ZA@HMNs of various concentrations ($n = 3$). (d) DCF fluorescence images of 4T1 cells receiving different treatments. Scale bars are 20 μm. ns > 0.05, *$p < 0.05$, **$p < 0.01$, ***$p < 0.001$.

signals within cytoplasm. The findings strongly demonstrate that the ZA@HMNs could be efficiently internalized by 4T1 cells upon CD44 receptor-mediated endocytosis. By contrast, in the presence of free HA segments, the cellular uptake of ZA@HMNs by 4T1 cells was impeded due to their competition with free HA segments for CD44 receptors of 4T1 cells. With the incubation time being prolonged from 1 to 4 h (Fig. 4b), the ICG fluorescence intensity of 4T1 cells treated with ICG-labeled ZA@HMNs was prominently boosted, illustrating the increased cellular uptake of these nanoparticles over time. Furthermore, due to the acidity/GSH-triggered disintegration of ZA@HMNs (Fig. 2b and f), undoubtedly, the endocytosed ZA@HMNs within an acidic and GSH-rich intracellular environment could further liberate ZA molecules and Fe^{3+} ions. It was anticipated that the ZA molecules released from ZA@HMNs could inhibit intracellular FPPS to induce cell apoptosis, while the liberated Fe^{3+} ions could produce •OH to elicit cell oxidative damage.

Encouraged by the sound GSH depletion ability, as observed in Fig. 3b, the capability of ZA@HMNs to consume intracellular GSH was further explored by DTNB assay. As revealed in Fig. 4c, the intracellular GSH level of 4T1 cells incubated with ZA@HMNs declined from 100 to 73.4 % with increasing concentration of ZA@HMNs from 0 to 200 μg/mL. This indicates that the ZA@HMNs internalized by 4T1 cells could somewhat deplete endogenous GSH by Fe^{2+}/Fe^{3+} redox couples (Scheme 1b). Next, the intracellular •OH generation performance of ZA@HMNs was evaluated by DCFH-DA assay. 4T1 cells incubated with ZA@HMNs at pH 7.4 exhibited appreciable DCF fluorescence signals compared to cells without any treatment as a control (Fig. 4d), signifying that the internalized ZA@HMNs converted intracellular H_2O_2 into •OH upon Fe^{3+}/Fe^{2+}-mediated Fenton reaction. Notably, the intracellular DCF fluorescence signals of the ZA@HMNs-treated 4T1 cells under weakly acidic conditions (pH 6.5) containing 100 μM H_2O_2 mimicking the tumor microenvironment were further enhanced, illustrating that

the ZA@HMNs promoted •OH production upon acidity-amplified Fenton reaction in the assist of H_2O_2. According to these results, the ZA@HMNs were anticipated to efficiently produce •OH under H_2O_2-rich and acidic tumor microenvironment to boost the anticancer effect of CDT.

3.4. Intracellular LPO generation and mitochondrial dysfunction

Recently, the CDT-mediated intracellular •OH generation, GSH depletion, and GPX4 downregulation have been proven to cause LPO accumulation, thus eliciting ferroptosis [53–55]. In light of the previously verified intracellular •OH generation and GSH consumption, the in vitro LPO production of ZA@HMNs in 4T1 cells was assessed using C11-BODIPY$^{581/591}$, an oxidation-sensitive and LPO-specific fluorescence probe. As presented in Fig. 5a, 4T1 cells incubated with HMNs or ZA@HMNs showed strong green fluorescence, whereas 4T1 cells exposed to free ZA molecules displayed quite weak green fluorescence. This suggests that the effective •OH generation and GSH depletion of HMNs and ZA@HMNs within 4T1 cells prominently promote LPO production, thereby starting ferroptosis. On the other hand, some studies point out that ferroptosis and over-generation of •OH can lead to oxidative injury to mitochondria and provoke the loss of mitochondrial membrane potential [55–57]. To further confirm the mitochondrial damage induced by ZA@HMNs in 4T1 cells, a potential-sensitive fluorescence probe JC-1 was used to detect mitochondrial dysfunction by the change from red fluorescence (JC-1 aggregate) to green fluorescence (JC-1 monomer). Compared to the control group, the free ZA group exhibited somewhat increased green fluorescence, indicating partial mitochondrial injury. This could be ascribed to that triphosphoric acid 1-adenosine-5¢-y l ester-[3-methylbut-3-enyl] ester (Apppi) from ZA-mediated FPPS inactivation interferes with mitochondrial ADP/ATP translocase, eliciting mitochondria to lose their membrane potential [19]. Notably, 4T1 cells treated with HMNs and ZA@HMNs showed appreciably enhanced green fluorescence and declined red fluoresce, in particular for ZA@HMNs (Fig. 5b). This suggests that the ZA@HMNs internalized by 4T1 cells largely cause mitochondrial dysfunction by LPO-triggered ferroptosis, ZA-induced FPPS inactivation and Fe^{2+}/Fe^{3+}-mediated •OH over-production.

3.5. In vitro chemo/chemodynamic combination therapy

To investigate the anticancer efficacy of ZA chemotherapy combined with HMNs-based CDT, the viability of 4T1 cells treated with ZA@HMNs was assessed by MTT assay. As presented in Fig. 6a, the viability of 4T1 cells receiving HMNs gradually declined from 92.6 to 74.1 % with increasing concentration of HMNs, indicating that the HMNs-mediated CDT could partly suppress the proliferation of 4T1 cells. Similarly, some studies also reported the anticancer effect of organometallic nanoparticles [58–62]. The viability of 4T1 cells incubated with free ZA molecules was slightly reduced when the ZA concentration was increased beyond 50 μM. Such a low cytotoxicity of free ZA molecules could be ascribed to poor cellular uptake due to their high hydrophilicity [21,63]. By contrast, the ZA@HMNs exhibited appreciable cytotoxicity against 4T1 cells in a concentration-dependent manner. Also, the ZA@HMNs displayed anticancer potency on 4T1 cells superior to HMNs. The fluorescence images of Calcein-AM/PI-stained 4T1 cells receiving different treatments revealed the mild anticancer effect of free ZA molecules and HMNs, respectively, as well as enhanced anticancer activity of ZA@HMNs (Figs. 6b and S9), being consistent with the results of MTT assay. These findings suggest that the active CD44-targeting capability of ZA@HMNs and their acidity/GSH-triggered ZA release could efficiently promote intracellular ZA delivery, thus enhancing anticancer efficacy by combining with HMNs-mediated CDT. In the last decade, increased studies have demonstrated that TAMs are the prominent components of tumor microenvironment in breast cancers and crucial tumor-promoting cells [18,22,64]. TAMs assist breast tumor growth, including cancer cell progression, invasion, and metastasis [65,66]. Therefore, TAMs have been considered as potential targets for breast cancer treatment. In light of that ZA has been verified to kill macrophages selectively, and CD44 receptors are presented on the TAMs [67], it is worth assessing the cytotoxicity of ZA@HMNs on the macrophage-like RAW 264.7 cell line used as a TAM model. Note that the viability of RAW 264.7 cells treated with free ZA molecules was remarkably declined with the increase of ZA concentration from 6.25 to 100 μM (Fig. 6c). Obviously, compared to 4T1 cells (Fig. 6a), RAW 264.7 cells were more sensitive to free ZA molecules. Importantly, the ZA@HMNs exhibited higher cytotoxicity on RAW 264.7 cells than free ZA molecules and HMNs. Based on the above findings, the ZA chemotherapy combined with Fe^{2+}/Fe^{3+}-mediated CDT delivered by ZA@HMNs showed superior capability of inhibiting the proliferation of 4T1 cells and RAW 264.7 cells, thus being expected to improve the treatment of breast tumors. Besides, Fig. 6d revealed that the healthy WS1 cells incubated with HMNs (12.5–200 μg/mL) exhibited high viability (over 90 %), indicating the few cytotoxicity of HMNs on normal cells.

3.6. In vivo biodistribution and tumor accumulation

The in vivo tumor accumulation and biodistribution of ZA@HMNs were further studied using the subcutaneous 4T1 tumor model in female BALB/c mice. Upon intravenous injection with free ICG molecules as the control and ICG-labeled ZA@HMNs, respectively, the in vivo ICG fluorescence images of 4T1 tumor-bearing mice were obtained at different time intervals. Note that the ICG fluorescence intensity in the tumor sites of the ICG-labeled ZA@HMN group was considerably higher than that of

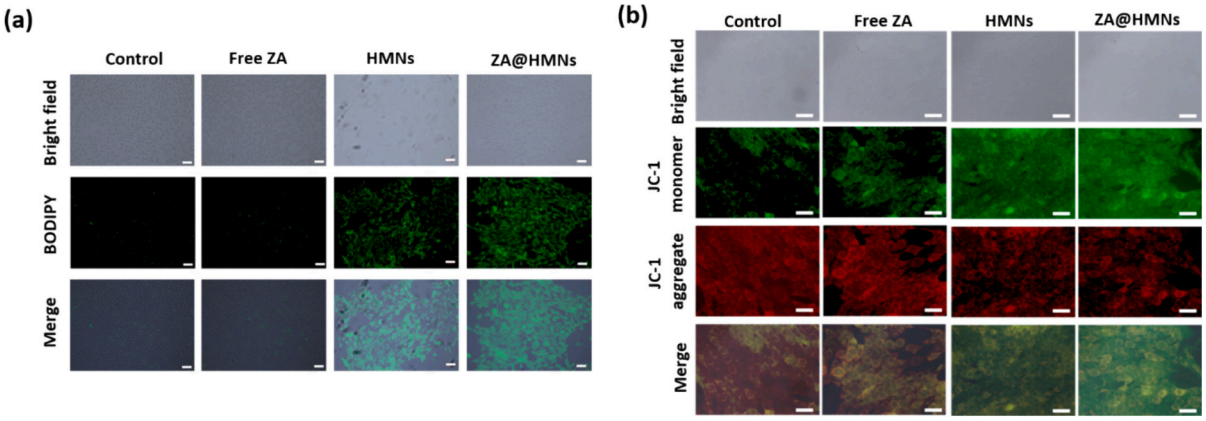

Fig. 5. (a) BODIPY™ 581/591 C11 staining and (b) JC-1 staining of 4T1 cells incubated with free ZA molecules, HMNs, and ZA@HMNs, respectively, at 37 °C for 24 h. Scale bars are 50 μm.

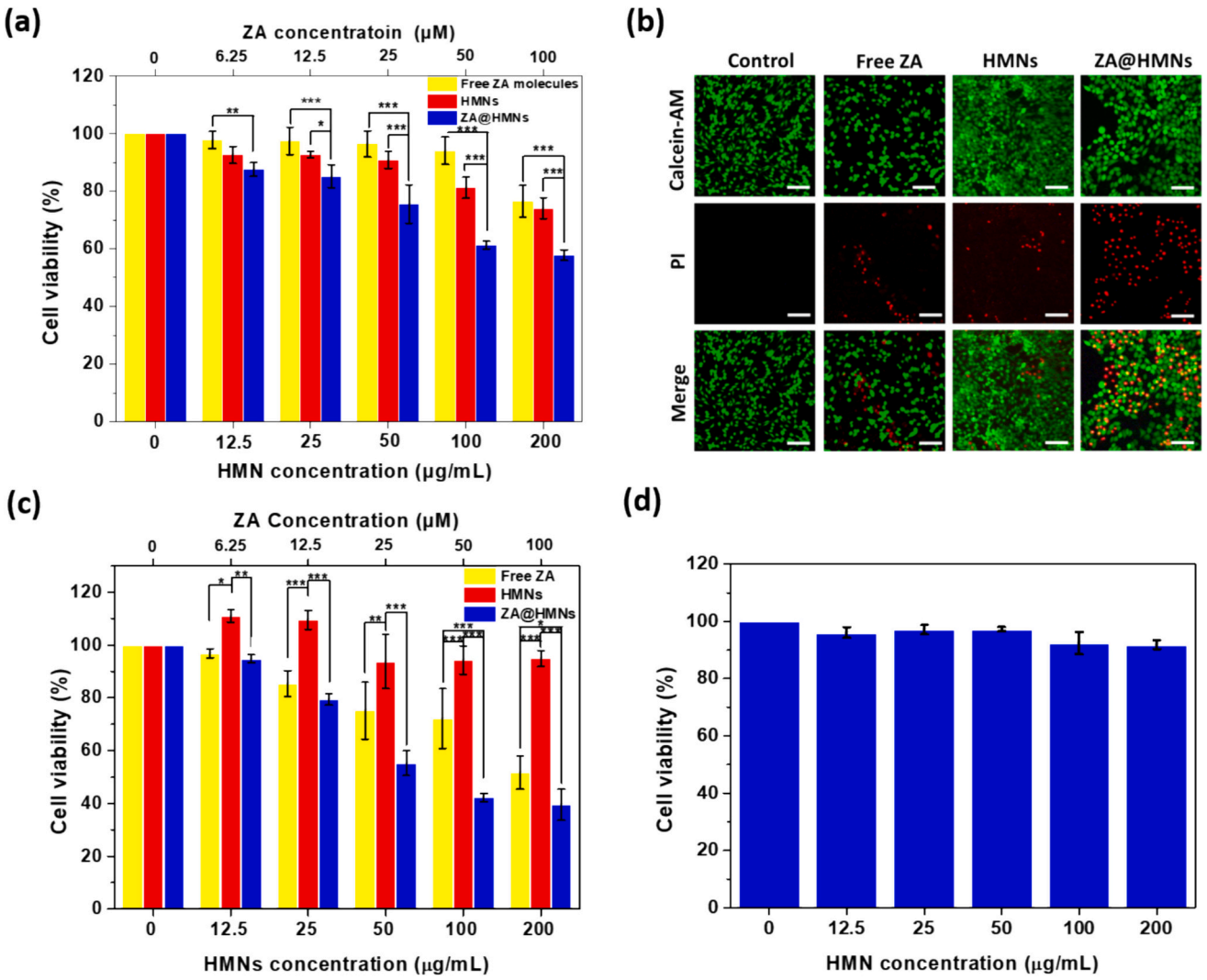

Fig. 6. (a) Cell viability ($n = 3$) and (b) calcein-AM/PI staining of 4T1 cells treated with free ZA molecules, HMNs and ZA@HMNs, respectively. The viable cells were stained with calcein-AM (green), and the dead cells were stained with PI (red). Scale bars are 200 μm. (c) Cell viability of RAW 264.7 cells treated with free ZA molecules, HMNs, and ZA@HMNs, respectively, at 37 °C for 24 h ($n = 3$). (d) Cell viability of WS1 cells incubated with HMNs at 37 °C for 48 h (n = 3). ns > 0.05, *$p < 0.05$, **$p < 0.01$, ***$p < 0.001$.

the free ICG group during the identical time period (Fig. 7a and b). Also, the ex vivo fluorescence intensity of tumors receiving ICG-labeled ZA@HMNs was appreciably stronger compared to that of tumors from free ICG groups (Fig. 7c and d). These results illustrate the promoted tumor deposition of ICG-labeled ZA@HMNs through the EPR effect and HA-mediated tumor targeting. In contrast, due to a lack of specific tumor targeting and self-aggregation, free ICG molecules were rapidly captured by the reticuloendothelial system (RES), thus showing poor tumor accumulation [49]. Furthermore, the ex vivo ICG fluorescence signals of livers of tumor-bearing mice treated with ICG-labeled ZA@HMNs were much higher in comparison with those of tumors and other organs, ascribing to the inevitable elimination of nanoparticles by the RES. Similar biodistribution of MOF-based nanoparticles in tumor-bearing mice has been reported in other studies [47,68,69].

3.7. *In vivo antitumor efficacy*

Encouraged by the satisfied tumor accumulation, the in vivo antitumor potency of ZA@HMNs was further evaluated using a 4T1 tumor-bearing mouse model (Fig. 8a). As presented in Fig. 8b, during the treatment process, the tumor volume of mice treated with ZA@HMNs was appreciably smaller than that of mice receiving either PBS as the control, free ZA or HMNs. In addition, 14 days after treatment, the relative tumor volume (V/V_o) of mice treated with ZA@HMNs was smaller compared to that of mice receiving either free ZA molecules or HMNs (Fig. 8c). In agreement with the results of the in vivo tumor growth inhibition, tumors harvested from the sacrificed mice treated with ZA@HMNs showed the smallest size and weight among the tumor receiving other treatments (Fig. 8d and e). Evidently, the combination of ZA chemotherapy and HMNs-mediated CDT delivered by the ZA@HMNs effectively suppressed tumor progress in comparison with the single ZA-based chemotherapy and HMNs-triggered CDT.

In order to further verify the prominent antitumor effects of ZA@HMNs, after 14-day treatment, the tumors of the mice were collected for H&E staining, and the Ki67 assay was also conducted to assess the proliferative capacity of the tumors. As revealed in Fig. 9, the H&E-stained tumor tissue of the ZA@HMN group exhibited severe nucleus shrinkage, plasmatorrhexis, and karyorrhexis, signifying an apoptosis of massive cancer cells. Moreover, Ki67 staining images showed that the proliferation of tumor cells receiving ZA@HMNs was largely inhibited compared to that of other treatment groups, which corresponded well to the therapeutic outcomes. On the other hand, to further confirm the ZA@HMNs-triggered ferroptosis, immunohistochemistry analysis of tumor sections for GPX4 (a biomarker of

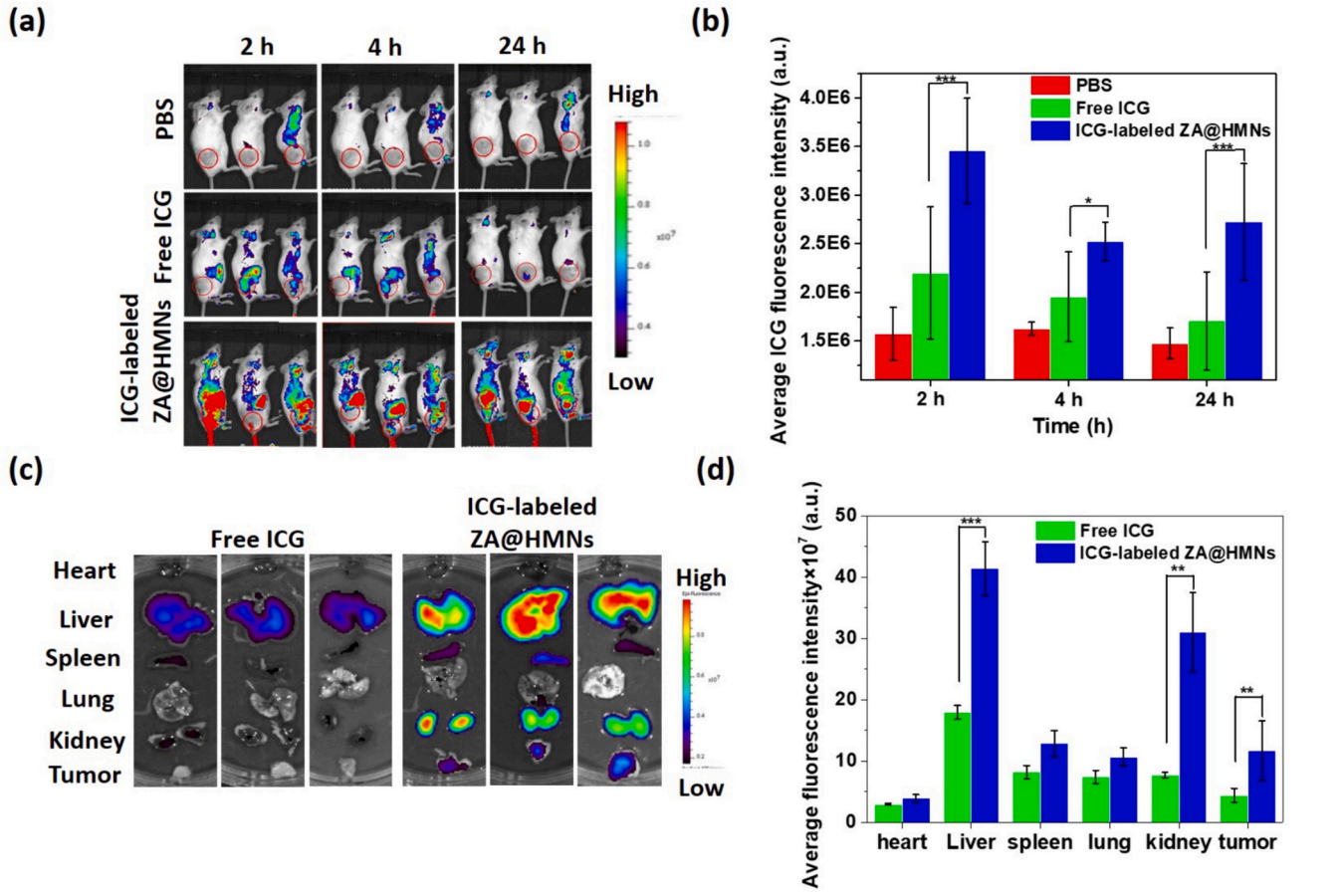

Fig. 7. (a) In vivo NIR fluorescence images and (b) ICG fluorescence signals of 4T1 tumor-bearing mice intravenously injected with PBS as the control, free ICG molecules or ICG-labeled ZA@HMNs (n = 3). The tumor sites were marked with red circles. (c) NIR fluorescence images and (d) average ICG fluorescence intensities of tumors and major organs at 24 h post-injection with free ICG molecules and ICG-labeled ZA@HMNs, respectively (n = 3). ns > 0.05, *$p < 0.05$, **$p < 0.01$, ***$p < 0.001$.

ferroptosis) was performed. As presented in the GPX4-stained images of tumor sections, the ZA@HMN group displayed significantly decreased GPX4 expression compared to other treatment groups. This demonstrates again that ZA@HMNs can effectively inhibit GPX4 expression by consuming GSH of tumor cells via the Fe^{2+}/Fe^{3+}-mediated redox process, thus promoting LPO accumulation to provoke ferroptosis.

The biocompatibility of ZA@HMNs was further evaluated. During the treatment process, no significant variation in body weight was observed in all treatment groups (Fig. S10), suggesting that the ZA@HMNs did not lead to serious acute toxicity. Also, as shown in H&E staining images of primary organs of mice receiving different treatments (Fig. S11), similar to the PBS group, the ZA@HMN groups showed little tissue histological damage and abnormality, indicating good in vivo biocompatibility and biosafety. Compared to normal tissue, 4T1 breast tumors are characterized by weak acidity and high GSH and H_2O_2 concentrations, which is beneficial for the acidity/GSH-triggered ZA and Fe^{3+} release of ZA@HMNs (Fig. 2h and i) and CDT. This signifies that the ZA@HMNs could exert tumor-specific treatment without severe adverse effects. All of the above findings demonstrated that the tumor-homing ZA@HMNs developed herein not only integrated ZA chemotherapy with CDT-elicited redox imbalance upon HMNs-mediated ·OH production and GSH depletion, thus leading to cell apoptosis and ferroptosis to efficiently retard tumor growth (Scheme 1b), but also maintained satisfied biosafety.

4. Conclusions

To boost the therapeutic outcomes of the chemo/chemodynamic therapy on breast cancer, in this study, the ZA@HMNs were fabricated by a simple and economical method. Distinct from that previous ZA delivery systems were prepared by using complicated materials and multiple-step approaches, and showed limited ZA loading content, the attained ZA@HMNs were characterized to have several outstanding properties, including (1) high ZA payload, (2) superior colloidal stability in serum-containing milieu, (3) acidity/GSH-triggered ZA and Fe^{3+} release, (4) moderate GSH consumption, (5) acidity-enhanced Fenton reaction and (6) active tumor targeting. The internalization of ZA@HMNs by 4T1 cells was effectively promoted through CD44-mediated endocytosis. Moreover, the ZA@HMNs efficiently depleted intracellular GSH via Fe^{3+}/Fe^{2+} redox process and converted endogenous H_2O_2 into •OH, thereby eliciting LPO and mitochondria dysfunction to cause cell death in the combined ferroptosis and ZA-induced chemotherapy manner. Furthermore, the ZA@HMNs exhibited potent cytotoxicity on the macrophage-like RAW 264.7 cells. Notably, the in vivo antitumor efficacy studies and ki67 and GPX4 staining of tumor sections demonstrated that compared to free ZA molecules and HMNs, the ZA@HMNs not only prominently inhibited 4T1 tumor growth by combining ZA chemotherapy with HMNs-mediated CDT/ferroptosis but also maintained acceptable biocompatibility. Therefore, this work offers a promising strategy for breast tumor-targeted chemo/chemodynamic therapy.

CRediT authorship contribution statement

Nien-Tzu Yeh: Project administration, Methodology, Investigation, Formal analysis, Data curation. **Tzu-Chen Lin:** Validation,

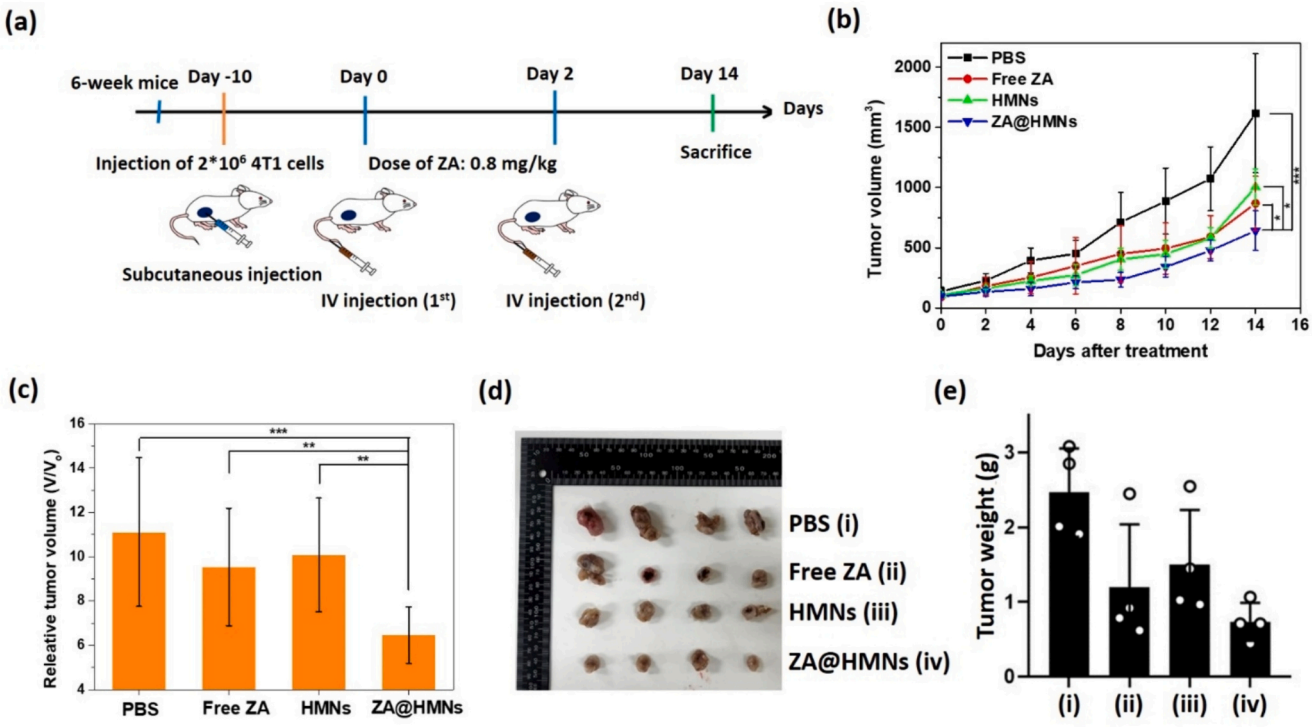

Fig. 8. (a) Schematic illustration for the experimental design for in vivo therapeutic evaluation in 4T1 tumor-bearing mice. (b) Tumor volume curves and (c) relative tumor volume (V/V_o) of 4T1 tumor-bearing mice receiving different treatments ($n = 4$). (d) Digital photographs and (e) weights of the tumors harvested from the euthanized mice after 14 days of treatment (n = 4). ns > 0.05, *p < 0.05, **p < 0.01, ***p < 0.001.

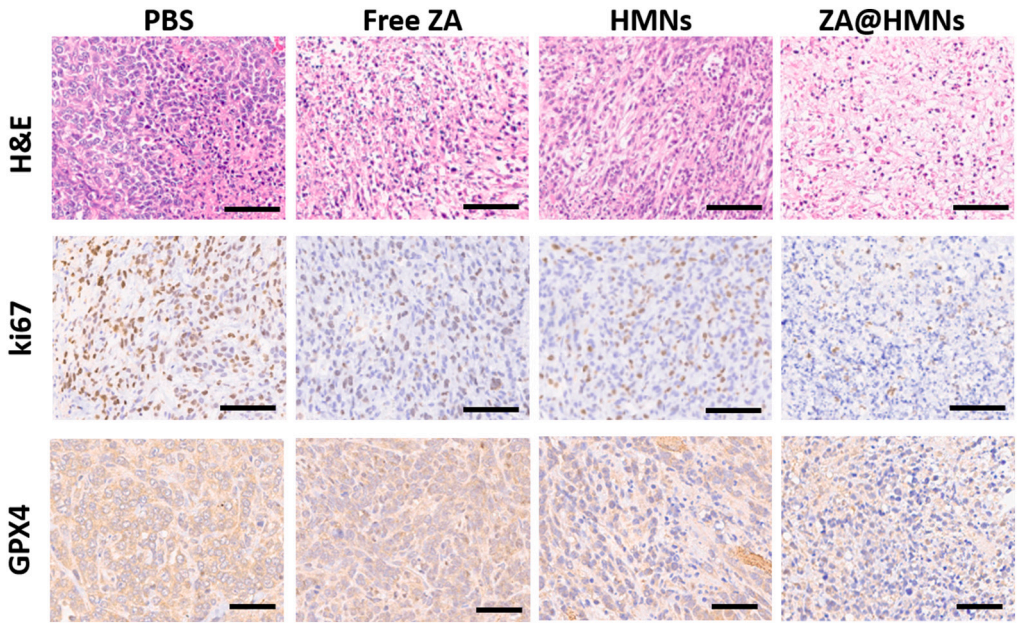

Fig. 9. H&E, Ki67, and GPX4 staining of tumor tissues from 4T1 tumor-bearing mice treated with free ZA molecules, HMNs, and ZA@HMNs, respectively. Scale bars of H&E and Ki67 staining images are 100 μm, while scale bars of GPX4 staining images are 50 μm.

Methodology, Investigation, Formal analysis. **I-Ju Liu:** Visualization, Methodology, Investigation. **Shang-Hsiu Hu:** Resources, Investigation, Conceptualization. **Tsai-Ching Hsu:** Supervision, Resources, Investigation. **Hao-Yang Chin:** Visualization, Methodology, Formal analysis. **Bor-Show Tzang:** Writing – original draft, Supervision, Investigation, Funding acquisition, Conceptualization. **Wen-Hsuan Chiang:** Writing – review & editing, Writing – original draft, Supervision, Project administration, Investigation, Funding acquisition, Conceptualization.

Declaration of competing interest

The authors declare that they have no known competing financial interests or personal relationships that could have appeared to influence the work reported in this paper.

Data availability

Data will be made available on request.

Acknowledgments

This work is supported by the National Science and Technology Council (MOST 111-2628-E-005-009-MY2; NSTC 113-2628-E-005-002-MY3), National Chung Hsing University and Chung Shan Medical University (NCHU-CSMU 11301), Taiwan.

Appendix A. Supplementary data

Supplementary data to this article can be found online at https://doi.org/10.1016/j.ijbiomac.2024.135271.

References

[1] S. Ahmad, S. Sayeed, N. Bano, K. Sheikh, K. Raza, In-silico analysis reveals quinic acid as a multitargeted inhibitor against cervical cancer, J. Biomol. Struct. Dyn. 41 (2023) 9770–9786, https://doi.org/10.1080/07391102.2022.2146202.
[2] S. Ahmad, K. Raza, Identification of 5-nitroindazole as a multitargeted inhibitor for CDK and transferase kinase in lung cancer: a multisampling algorithm-based structural study, Mol. Divers. 28 (2024) 1189–1202, https://doi.org/10.1007/s11030-023-10648-0.
[3] Global cancer burden growing, amidst mounting need for services, Saudi Med. J. 45 (2024) 326–327.
[4] A. Sahu, S. Ahmad, K. Imtiyaz, A.K. Kumaran, M. Islam, K. Raza, M. Easwaran, A. K. Kunnath, M.A. Rizvi, S. Verma, In-silico and in-vitro study reveals ziprasidone as a potential aromatase inhibitor against breast carcinoma, Sci. Rep. 13 (2023) 16545, https://doi.org/10.1038/s41598-023-43789-1.
[5] S. Ahmad, V. Singh, H.K. Gautam, K. Raza, Multisampling-based docking reveals imidazolidinyl urea as a multitargeted inhibitor for lung cancer: an optimization followed multi-simulation and in-vitro study, J. Biomol. Struct. Dyn. 42 (2024) 2494–2511, https://doi.org/10.1080/07391102.2023.2209673.
[6] W. Irvin, H.B. Muss, D.K. Mayer, Symptom management in metastatic breast cancer, Oncologist 16 (2011) 1203–1214, https://doi.org/10.1634/theoncologist.2011-0159.
[7] F. Benyettou, M. Alhashimi, M. O'Connor, R. Pasricha, J. Brandel, H. Traboulsi, J. Mazher, J.C. Olsen, A. Trabolsi, Sequential delivery of doxorubicin and zoledronic acid to breast cancer cells by CB[7]-modified iron oxide nanoparticles, ACS Appl. Mater. Interfaces 9 (2017) 40006–40016, https://doi.org/10.1021/acsami.7b11423.
[8] R.E. Coleman, M.C. Winter, D. Cameron, R. Bell, D. Dodwell, M.M. Keane, M. Gil, D. Ritchie, J.L. Passos-Coelho, D. Wheatley, R. Burkinshaw, S.J. Marshall, H. Thorpe, The effects of adding zoledronic acid to neoadjuvant chemotherapy on tumour response: exploratory evidence for direct anti-tumour activity in breast cancer, Br. J. Cancer 102 (2010) 1099–1105, https://doi.org/10.1038/sj.bjc.6605604.
[9] K. McKeage, G.L. Plosker, Zoledronic acid: a pharmacoeconomic review of its use in the management of bone metastases, Pharmacoeconomics 26 (2008) 251–268, https://doi.org/10.2165/00019053-200826030-00007.
[10] B. Wang, Y. Zhan, L. Yan, D. Hao, How zoledronic acid improves osteoporosis by acting on osteoclasts, Front. Pharmacol. 13 (2022) 961941, https://doi.org/10.3389/fphar.2022.961941.
[11] J. Zekri, M. Mansour, S.M. Karim, The anti-tumour effects of zoledronic acid, J. Bone Oncol. 3 (2014) 25–35, https://doi.org/10.1016/j.jbo.2013.12.001.
[12] J.R. Green, Bisphosphonates: preclinical review, Oncologist 9 (2004) 3–13, https://doi.org/10.1634/theoncologist.9-90004-3.
[13] K.M. Au, A. Satterlee, Y. Min, X. Tian, Y.S. Kim, J.M. Caster, L. Zhang, T. Zhang, L. Huang, A.Z. Wang, Folate-targeted pH-responsive calcium zoledronate nanoscale metal-organic frameworks: turning a bone antiresorptive agent into an anticancer therapeutic, Biomaterials 82 (2016) 178–193, https://doi.org/10.1016/j.biomaterials.2015.12.018.
[14] Early Breast Cancer Trialists' Collaborative Group (EBCTCG), Adjuvant bisphosphonate treatment in early breast cancer: meta-analyses of individual patient data from randomised trials, Lancet 386 (2015) 1353–1361, https://doi.org/10.1016/S0140-6736(15)60908-4.
[15] W. Zhang, X.D. Zhu, H.C. Sun, Y.Q. Xiong, P.Y. Zhuang, H.X. Xu, L.Q. Kong, L. Wang, W.Z. Wu, Z.Y. Tang, Depletion of tumor-associated macrophages enhances the effect of sorafenib in metastatic liver cancer models by antimetastatic and antiangiogenic effects, Clin. Cancer Res. 16 (2010) 3420–3430, https://doi.org/10.1158/1078-0432.CCR-09-2904.
[16] G. De Rosa, G. Misso, G. Salzano, M. Caraglia, Bisphosphonates and cancer: what opportunities from nanotechnology? J. Drug Deliv. 2013 (2013) 637976 https://doi.org/10.1155/2013/637976.
[17] S. Sousa, S. Auriola, J. Mönkkönen, J. Määttä, Liposome encapsulated zoledronate favours M1-like behaviour in murine macrophages cultured with soluble factors from breast cancer cells, BMC Cancer 15 (2015) 4, https://doi.org/10.1186/s12885-015-1005-7.
[18] X. Tang, D. Sui, M. Liu, H. Zhang, M. Liu, S. Wang, D. Zhao, W. Sun, M. Liu, X. Luo, X. Lai, X. Liu, Y. Deng, Y. Song, Targeted delivery of zoledronic acid through the sialic acid-siglec axis for killing and reversal of M2 phenotypic tumor-associated macrophages-a promising cancer immunotherapy, Int. J. Pharm. 590 (2020) 119929, https://doi.org/10.1016/j.ijpharm.2020.119929.
[19] S. Fathi-karkan, M. Zeeshan, M. Qindeel, R.E. Malekshah, A. Rahdar, L.F. R. Ferreira, NPs loaded with zoledronic acid as an advanced tool for cancer therapy, J. Drug Deliv. Sci. Technol. 87 (2023) 104805, https://doi.org/10.1016/j.jddst.2023.104805.
[20] Y.H. Chou, Y.L. Liu, T.C. Hsu, J.L. Yow, B.S. Tzang, W.H. Chiang, Tumor acidity-responsive polymeric nanoparticles to promote intracellular delivery of zoledronic acid by PEG detachment and positive charge exposure for enhanced antitumor potency, J. Mater. Chem. B 10 (2022) 4363–4374, https://doi.org/10.1039/D2TB00695B.
[21] Y.L. Liu, T.H. Wang, N.T. Yeh, W.J. Huang, B.S. Tzang, I.T. Wu, H.Y. Chin, S.H. Hu, T.C. Hsu, W.H. Chiang, Tumor-activated targetable photothermal chemotherapy using IR780/zoledronic acid-containing hybrid polymeric nanoassemblies with folate modification to treat aggressive breast cancer, Nanoscale 16 (2024) 1415–1427, https://doi.org/10.1039/D3NR05637F.
[22] X. Li, S.A. Valdes, R.F. Alzhrani, S. Hufnagel, S.D. Hursting, Z. Cui, Zoledronic acid-containing nanoparticles with minimum premature release show enhanced activity against extraskeletal tumor, ACS Appl. Mater. Interfaces 11 (2019) 7311–7319, https://doi.org/10.1021/acsami.8b16588.
[23] G. Salzano, S. Zappavigna, A. Luce, N. D'Onofrio, M.L. Balestrieri, A. Grimaldi, S. Lusa, D. Ingrosso, S. Artuso, M. Porru, C. Leonetti, M. Caraglia, G. De Rosa, Transferrin-targeted nanoparticles containing zoledronic acid as a potential tool to inhibit glioblastoma growth, J. Biomed. Nanotechnol. 12 (2016) 811–830, https://doi.org/10.1166/jbn.2016.2214.
[24] M. McClung, Bisphosphonates, Arq. Bras. Endocrinol. Metabol. 50 (2006) 735–744, https://doi.org/10.1590/S0004-27302006000400018.
[25] Y. Hattori, J. Yamashita, C. Sakaida, K. Kawano, E. Yonemochi, Evaluation of antitumor effect of zoledronic acid entrapped in folate-linked liposome for targeting to tumor-associated macrophages, J. Liposome Res. 25 (2015) 131–140, https://doi.org/10.3109/08982104.2014.954128.
[26] W. Yao, H. Xu, Y. Chen, Y. Xu, F. Zhou, Z. Wang, X. Cai, Mannose modified co-loaded zoledronic liposomes deplete M2-tumor-associated macrophages to enhance anti-tumor effect of doxorubicin on TNBC, J. Drug Deliv. Sci. Technol. 74 (2022) 103551, https://doi.org/10.1016/j.jddst.2022.103551.
[27] X. Li, Y.W. Naguib, Z. Cui, In vivo distribution of zoledronic acid in a bisphosphonate-metal complex-based nanoparticle formulation synthesized by a reverse microemulsion method, Int. J. Pharm. 526 (2017) 69–76, https://doi.org/10.1016/j.ijpharm.2017.04.053.
[28] Y. Pang, Y. Fu, C. Li, Z. Wu, W. Cao, X. Hu, X. Sun, W. He, X. Cao, D. Ling, Q. Li, C. Fan, C. Yang, X. Kong, A. Qin, Metal-organic framework nanoparticles for ameliorating breast cancer-associated osteolysis, Nano Lett. 20 (2020) 829–840, https://doi.org/10.1021/acs.nanolett.9b02916.
[29] A. Dehnoee, R.J. Kalbasi, M.M. Zangeneh, M.-R. Delnavazi, A. Zangeneh, One-step synthesis of silver nanostructures using Heracleum persicum fruit extract, their cytotoxic activity, anti-cancer and anti-oxidant activities, Micro, Nano Lett. 18 (2022) 1–11, https://doi.org/10.1049/mna2.12153.
[30] L. Ma, A. Ahmeda, K. Wang, A.R. Jalalvand, K. Sadrjavadi, M. Nowrozi, A. Zangeneh, M.M. Zangeneh, X. Wang, Introducing a novel chemotherapeutic drug formulated by iron nanoparticles for the clinical trial studies, Appl. Organomet. Chem. 36 (2022) 5498, https://doi.org/10.1002/aoc.5498.
[31] H. Zhao, H. Su, A. Ahmeda, Y. Sun, Z. Li, M.M. Zangeneh, M. Nowrozi, A. Zangeneh, R. Moradi, Biosynthesis of copper nanoparticles using allium eriophyllum Boiss leaf aqueous extract; characterization and analysis of their antimicrobial and cutaneous wound-healing potentials, Appl. Organomet. Chem. 36 (2022) 5587, https://doi.org/10.1002/aoc.5587.
[32] G. Wang, A. Ahmeda, Z. Malek, S. Mansooridara, A. Zangeneh, M.M. Zangeneh, Chemical characterization and therapeutic properties of Achillea biebersteinii leaf aqueous extract synthesized copper nanoparticles against methamphetamine-induced cell death in PC12: a study in the nanotechnology and neurology fields, Appl. Organomet. Chem. 34 (2020) 5488, https://doi.org/10.1002/aoc.5488.
[33] A. Dehnoee, R. Javad Kalbasi, M.M. Zangeneh, M.-R. Delnavazi, A. Zangeneh, Characterization, anti-lung cancer activity, and cytotoxicity of bio-synthesized copper nanoparticles by thymus fedtschenkoi leaf extract, J. Clust. Sci. 35 (2024) 863–874, https://doi.org/10.1007/s10876-023-02512-w.
[34] B.N. Yalamandala, W.T. Shen, S.H. Min, W.H. Chiang, S.J. Chang, S.H. Hu, Advances in functional metal-organic frameworks based on-demand drug delivery systems for tumor therapeutics, Adv. Nanobiomed. Res. 1 (2021) 2100014, https://doi.org/10.1002/anbr.202100014.
[35] X.X. Yang, X. Xu, M.F. Wang, H.Z. Xu, X.C. Peng, N. Han, T.T. Yu, L.G. Li, Q.R. Li, X. Chen, Y. Wen, T.F. Li, A nanoreactor boosts chemodynamic therapy and ferroptosis for synergistic cancer therapy using molecular amplifier dihydroartemisinin, J. Nanobiotechnol. 20 (2022) 230, https://doi.org/10.1186/s12951-022-01455-0.
[36] Z. Mo, X. Pan, X. Pan, L. Ye, H. Hu, Q. Xu, X. Hu, Z. Xu, J. Xiong, G. Liao, S. Yang, MOF(Fe)-derived composites as a unique nanoplatform for chemo-photodynamic tumor therapy, J. Mater. Chem. B 10 (2022) 8760–8770, https://doi.org/10.1039/D2TB01691E.
[37] B. Wang, Y. Dai, Y. Kong, W. Du, H. Ni, H. Zhao, Z. Sun, Q. Shen, M. Li, Q. Fan, Tumor microenvironment-responsive Fe(III)-porphyrin nanotheranostics for tumor imaging and targeted chemodynamic-photodynamic therapy, ACS Appl. Mater. Interfaces 12 (2020) 53634–53645, https://doi.org/10.1021/acsami.0c14046.

[38] C. Wu, D. Xu, M. Ge, J. Luo, L. Chen, Z. Chen, Y. You, Y.X. Zhu, H. Lin, J. Shi, Blocking glutathione regeneration: inorganic NADPH oxidase nanozyme catalyst potentiates tumoral ferroptosis, Nano Today 46 (2022) 101574, https://doi.org/10.1016/j.nantod.2022.101574.
[39] L. Zhong, L. Xu, Y. Liu, Q. Li, D. Zhao, Z. Li, H. Zhang, H. Zhang, Q. Kan, Y. Wang, J. Sun, Z. He, Transformative hyaluronic acid-based active targeting supramolecular nanoplatform improves long circulation and enhances cellular uptake in cancer therapy, Acta Pharm. Sin. B 9 (2019) 397–409, https://doi.org/10.1016/j.apsb.2018.11.006.
[40] K. Hu, H. Zhou, Y. Liu, Z. Liu, J. Liu, J. Tang, J. Li, J. Zhang, W. Sheng, Y. Zhao, Y. Wu, C. Chen, Hyaluronic acid functional amphipathic and redox-responsive polymer particles for the co-delivery of doxorubicin and cyclopamine to eradicate breast cancer cells and cancer stem cells, Nanoscale 7 (2015) 8607–8618, https://doi.org/10.1039/C5NR01084E.
[41] J.Y. Oh, Y. Sim, G. Yang, M.H. Park, K. Kim, J.H. Ryu, Surface functionalization of metal-organic framework nanoparticle for overcoming biological barrier in cancer therapy, Inorg. Chem. Front. 11 (2024) 3119–3135, https://doi.org/10.1039/D4QI00523F.
[42] C. Qiao, R. Zhang, Y. Wang, Q. Jia, X. Wang, Z. Yang, T. Xue, R. Ji, X. Cui, Z. Wang, Rabies virus-inspired metal-organic frameworks (MOFs) for targeted imaging and chemotherapy of glioma, Angew. Chem. Int. Ed. Eng. 59 (2020) 16982–16988, https://doi.org/10.1002/anie.202007474.
[43] B. Yang, L. Ding, H. Yao, Y. Chen, J. Shi, A metal-organic framework (MOF) Fenton nanoagent-enabled nanocatalytic cancer therapy in synergy with autophagy inhibition, Adv. Mater. 32 (2020) 1907152, https://doi.org/10.1002/adma.201907152.
[44] F. Shu, D. Lv, X.L. Song, B. Huang, C. Wang, Y. Yu, S.C. Zhao, Fabrication of a hyaluronic acid conjugated metal organic framework for targeted drug delivery and magnetic resonance imaging, RSC Adv. 8 (2018) 6581–6589, https://doi.org/10.1039/C7RA12969F.
[45] X. Chen, S.M. Argandona, F. Melle, N. Rampal, D. Fairen-Jimenez, Advances in surface functionalization of next-generation metal-organic frameworks for biomedical applications: design, strategies, and prospects, Chem 10 (2024) 504–543, https://doi.org/10.1016/j.chempr.2023.09.016.
[46] X. Di, Z. Pei, Y. Pei, T.D. James, Tumormicroenvironment-oriented MOFs for chemodynamic therapy, Coord. Chem. Rev. 484 (2023) 215098, https://doi.org/10.1016/j.ccr.2023.215098.
[47] D. Wang, J. Zhou, R. Chen, R. Shi, G. Xia, S. Zhou, Z. Liu, N. Zhang, H. Wang, Z. Guo, Q. Chen, Magnetically guided delivery of DHA and Fe ions for enhanced cancer therapy based on pH-responsive degradation of DHA-loaded Fe_3O_4@C@MIL-100(Fe) nanoparticles, Biomaterials 107 (2016) 88–101, https://doi.org/10.1016/j.biomaterials.2016.08.039.
[48] Y. Ding, Y. Dai, M. Wu, L. Li, Glutathione-mediated nanomedicines for cancer diagnosis and therapy, Chem. Eng. J. 426 (2021) 128880, https://doi.org/10.1016/j.cej.2021.128880.
[49] T.H. Wang, M.Y. Shen, N.T. Yeh, Y.H. Chen, T.C. Hsu, H.Y. Chin, Y.T. Wu, B. S. Tzang, W.H. Chiang, Photothermal nanozymes to self-augment combination cancer therapy by dual-glutathione depletion and hyperthermia/acidity-activated hydroxyl radical generation, J. Colloid Interface Sci. 650 (2023) 1698–1714, https://doi.org/10.1016/j.jcis.2023.07.134.
[50] F. Liu, L. Lin, Y. Zhang, Y. Wang, S. Sheng, C. Xu, H. Tian, X. Chen, A tumor-microenvironment-activated nanozyme-mediated theranostic nanoreactor for imaging-guided combined tumor therapy, Adv. Mater. 31 (2019) 1902885, https://doi.org/10.1002/adma.201902885.
[51] L.S. Lin, J. Song, L. Song, K. Ke, Y. Liu, Z. Zhou, Z. Shen, J. Li, Z. Yang, W. Tang, Simultaneous Fenton-like ion delivery and glutathione depletion by MnO_2-based nanoagent to enhance chemodynamic therapy, Angew. Chem. Int. Ed. 57 (2018) 4902–4906, https://doi.org/10.1002/anie.201712027.
[52] W. Chen, J. Liu, C. Zheng, Q. Bai, Q. Gao, Y. Zhang, K. Dong, T. Lu, Research progress on improving the efficiency of CDT by exacerbating tumor acidification, Int. J. Nanomedicine 17 (2022) 2611–2628, https://doi.org/10.2147/IJN.S366187.
[53] C. Liang, X. Zhang, M. Yang, X. Dong, Recent progress in ferroptosis inducers for cancer therapy, Adv. Mater. 31 (2019) 1904197, https://doi.org/10.1002/adma.201904197.
[54] T. Liu, W. Liu, M. Zhang, W. Yu, F. Gao, C. Li, S.B. Wang, J. Feng, X.Z. Zhang, Ferrous-supply-regeneration nanoengineering for cancer-cell-specific ferroptosis in combination with imaging-guided photodynamic therapy, ACS Nano 12 (2018) 12181–12192, https://doi.org/10.1021/acsnano.8b05860.
[55] Z. Liu, S. Liu, B. Liu, Y. Bian, M. Yuan, C. Yang, Q. Meng, C. Chen, P. Ma, J. Lin, Fe (III)-naphthazarin metal-phenolic networks for glutathione-depleting enhanced ferroptosis-apoptosis combined cancer therapy, Small 19 (2023) 2207825, https://doi.org/10.1002/smll.202207825.
[56] J. Li, Y.C. Jia, Y.X. Ding, J. Bai, F. Cao, F. Li, The crosstalk between ferroptosis and mitochondrial dynamic regulatory networks, Int. J. Biol. Sci. 19 (2023) 2756–2771. https://www.ijbs.com/v19p2756.htm.
[57] Y. Liu, S. Lu, L.L. Wu, L. Yang, L. Yang, J. Wang, The diversified role of mitochondria in ferroptosis in cancer, Cell Death Dis. 14 (2023) 519, https://doi.org/10.1038/s41419-023-06045-y.
[58] J. Bai, X. Gongsun, L. Xue, M.M. Zangeneh, Introducing a modern chemotherapeutic drug formulated by iron nanoparticles for the treatment of human lung cancer, J. Exp. Nanosci. 16 (2021) 397–409, https://doi.org/10.1080/17458080.2021.1998460.
[59] Y. Li, N. Li, W. Jiang, G. Ma, M.M. Zangeneh, In situ decorated Au NPs on pectin-modified Fe3O4 NPs as a novel magnetic nanocomposite (Fe_3O_4/Pectin/Au) for catalytic reduction of nitroarenes and investigation of its anti-human lung cancer activities, Int. J. Biol. Macromol. 163 (2020) 2162–2171, https://doi.org/10.1016/j.ijbiomac.2020.09.102.
[60] J. Liu, A. Zangeneh, M.M. Zangeneh, B. Guo, Antioxidant, cytotoxicity, anti-human esophageal squamous cell carcinoma, anti-human Caucasian esophageal carcinoma, anti-adenocarcinoma of the gastroesophageal junction, and anti-distal esophageal adenocarcinoma properties of gold nanoparticles green synthesized by Rhus coriaria L. fruit aqueous extract, J. Exp. Nanosci. 15 (2020) 202–216, https://doi.org/10.1080/17458080.2020.1766675.
[61] A. Ahmeda, M.M. Zangeneh, A. Zangeneh, Green formulation and chemical characterization of Lens culinaris seed aqueous extract conjugated gold nanoparticles for the treatment of acute myeloid leukemia in comparison to mitoxantrone in a leukemic mouse model, Appl. Organomet. Chem. 34 (2020) 5369, https://doi.org/10.1002/aoc.5369.
[62] A. Ahmeda, A. Zangeneh, M.M. Zangeneh, Green synthesis and chemical characterization of gold nanoparticle synthesized using Camellia sinensis leaf aqueous extract for the treatment of acute myeloid leukemia in comparison to daunorubicin in a leukemic mouse model, Appl. Organomet. Chem. 34 (2020) 5290, https://doi.org/10.1002/aoc.5290.
[63] M.R. Webster, C. Kamat, N. Connis, M. Zhao, A.T. Weeraratna, M.A. Rudek, C. L. Hann, C.L. Freel Meyers, Bisphosphonamidate clodronate prodrug exhibits selective cytotoxic activity against melanoma cell lines, Mol. Cancer Ther. 13 (2014) 297–306, https://doi.org/10.1158/1535-7163.MCT-13-0315.
[64] X. Huang, J. Cao, X. Zu, Tumor-associated macrophages: an important player in breast cancer progression, Thorac. Cancer 13 (2022) 269–276, https://doi.org/10.1111/1759-7714.14268.
[65] J. Choi, J. Gyamfi, H. Jang, J.S. Koo, The role of tumor-associated macrophage in breast cancer biology, Histol. Histopathol. 33 (2018) 133–145, https://doi.org/10.14670/HH-11-916.
[66] Y. Chen, Y. Song, W. Du, L. Gong, H. Chang, Z. Zou, Tumor-associated macrophages: an accomplice in solid tumor progression, J. Biomed. Sci. 26 (2019) 78, https://doi.org/10.1186/s12929-019-0568-z.
[67] J.M. Rios de la Rosa, A. Tirella, A. Gennari, I.J. Stratford, N. Tirelli, The CD44-mediated uptake of hyaluronic acid-based carriers in macrophages, Adv. Healthc. Mater. 6 (2017) 1601012, https://doi.org/10.1002/adhm.201601012.
[68] H. Deng, J. Zhang, Y. Yang, J. Yang, Y. Wei, S. Ma, Q. Shen, Chemodynamic and photothermal combination therapy based on dual-modified metal-organic framework for inducing tumor ferroptosis/pyroptosis, ACS Appl. Mater. Interfaces 14 (2022) 24089–24101, https://doi.org/10.1021/acsami.2c00574.
[69] X. Zhang, Y. Lu, D. Jia, W. Qiu, X. Ma, X. Zhang, Z. Xu, F. Wen, Acidic microenvironment responsive polymeric MOF-based nanoparticles induce immunogenic cell death for combined cancer therapy, J. Nanobiotechnol. 19 (2021) 455, https://doi.org/10.1186/s12951-021-01217-4.